# A Variational Method for Analyzing Vortex Flows in Radar-Scanned Tornadic Mesocyclones. Part II: Tests with Analytically Formulated Vortices

QIN XU[a] AND LI WEI[b]

[a] *NOAA/OAR/National Severe Storms Laboratory, Norman, Oklahoma*
[b] *Cooperative Institute for Mesoscale Meteorological Studies, University of Oklahoma, Norman, Oklahoma*

(Manuscript received 24 May 2020, in final form 4 January 2021)

ABSTRACT: The variational method formulated in Part I for analyzing vortex flow (VF), called VF-Var, is tested with simulated radar radial-velocity observations from idealized and pseudo-operational Doppler scans of analytically formulated benchmark vortices with spiral-band structures to resemble VFs in observed tornadic mesocyclones. The idealized Doppler scans are unidirectional in parallel along horizontal grid lines of a coarse-resolution grid, so they measure only the horizontal components of three-dimensional velocities in the analysis domain. The pseudo-operational Doppler scans mimic a scan mode used by operational WSR-88Ds for severe storms. Paired numerical experiments are designed and performed to test the two-step analysis versus single-step analysis formulated in VF-Var. Both analyses perform very well with dual-Doppler scans and reasonably well with single-Doppler scans. Errors in the analyzed velocities from single-Doppler scans are mainly in the unobserved velocity components and only in fractions of the benchmark velocities. When the vortex is upright or slanted in the direction perpendicular to idealized single-Doppler scans, the two-step analysis slightly outperforms the single-step analysis for idealized Doppler scans and pseudo-operational dual-Doppler scans. When the vortex becomes slanted in the direction largely along or against Doppler scans, both analyses become less (more) accurate in analyzing the horizontal (slantwise vertical) velocity, and the single-step analysis outperforms the two-step analysis especially for single-Doppler scans. By considering the projections of analyzed velocity on radar beams in the original Cartesian coordinates, useful insights are gained for understanding why and how the analysis accuracies are affected by vortex slanting.

KEYWORDS: Vortices; Radars/Radar observations; Variational analysis; Data assimilation

## 1. Introduction

Three-dimensional (3D) and 3.5D variational methods were developed at the National Severe Storms Laboratory (Gao et al. 2013; Xu et al. 2010, 2015a) to analyze storm winds from radar radial-velocity observations. Although these methods were shown to be useful for severe weather detections/warnings and related nowcast applications, they all have an intrinsic limitation for analyzing vortex winds in radar-observed mesocyclones due to the absence of vortex-flow dependence in their background error covariance formulations. To overcome this intrinsic limitation, vortex-flow-dependent covariance functions were formulated in a vortex-following moving frame to construct the background error covariance matrix in the recently developed two-dimensional (2D) variational method (Xu et al. 2015b). This 2DVar was shown to be effective and efficient for analyzing the horizontal winds within a vortex at lower elevations in tornadic mesocyclones scanned from either a single-Doppler radar or dual-Doppler radars for nowcast applications. To extend this 2DVar into a 3DVar for analyzing the 3D vortex flow (VF) in a radar-observed tornadic mesocyclone, it is necessary to accomplish the following two tasks. (i) The vortex center must be estimated first as a continuous function of height and time in the 4D space; a three-step method was developed for this (Xu et al. 2017). (ii) VF-dependent background error covariance functions must be formulated in a moving 3D coordinate system in which the vertical coordinate is given by the estimated vortex center axis and thus is slantwise curvilinear in general. This task is accomplished in the newly formulated 3DVar for VF analyses (Xu 2021, hereafter Part I), called VF-Var hereafter.

As a follow-up of Part I, this paper designs and performs numerical experiments to test the VF-Var with simulated radial-velocity observations from single-Doppler and dual-Doppler scans of analytically formulated vortices and examines the test results. In the VF-Var, the VF is partitioned into an axisymmetric part and the remaining asymmetric part. As shown in Fig. 4 of Part I, the axisymmetric part can be analyzed, either separately in the first step (and thus leave the asymmetric part analyzed in the second step) or jointly with the asymmetric part in a single step. The two-step and single-step approaches will be tested with simulated radar radial-velocity observations, and their performances will be examined and compared for various different cases.

The paper is organized as follows: Section 2 describes the benchmark VF (formulated analytically in appendix A and used as truth for testing the VF-Var) and the radial-velocity observations generated from idealized and pseudo-operational Doppler scans of benchmark vortices. Section 3 sets the parameter values for background error covariance functions and designs numerical experiments for testing the VF-Var. Sections 4 and 5 present/examine the results of experiments performed with idealized Doppler scans and

*Corresponding author*: Dr. Qin Xu, qin.xu@noaa.gov

DOI: 10.1175/JAS-D-20-0159.1

pseudo-operational Doppler scans, respectively. Conclusions follow in section 6.

## 2. Benchmark VF and simulated radial-velocity observations

### a. Benchmark VF

The benchmark VF is configured analytically in appendix A, which is an one-cell vortex intended to resemble a large intense tornadic mesocyclone. As this benchmark VF is configured analytically as a spatially continuous vector field in the vortex-following coordinate system $(x', y', z', t')$ [see (2.1) and Fig. 1a of Part I], it can be used to evaluate the accuracies of analyzed VFs for differently slanted vortices to any required high spatial resolutions (because the analyzed VF is also a spatially continuous vector field as explained at the end of section 4 of Part I).

For the axisymmetric part of benchmark VF, the scalar field of tangential velocity $V_T^s$ and the vector field of slantwise vertical circulation expressed by $(V_R^s, w^s)$ in $(R, z')$ are plotted by blue contours and black arrows, respectively, in Fig. 1a, where $(R, z')$ is the vertical cross section for any given $\beta$ in the slantwise cylindrical coordinate system $(R, \beta, z')$ transformed from $(x', y', z')$ [see (2.4) of Part I]. From (A1a), (A2a), and (A2b), it is easy to see that the vertical variations of $V_T^s$, $V_R^s$, and $w^s$ shown in Fig. 1a are governed by $1 + 0.5\tanh(z'/h)$, $[\cosh(z'/h)]^{-2}/\rho_a$ and $\tanh(z'/h)/\rho_a$, respectively.

The asymmetric part of VF is formulated as a vector function of $(R, \beta, z')$ in terms of $(V_T^a, V_R^a, w^a)$ in (A4). As explained in appendix A, this asymmetric part contains no axisymmetric part and therefore is purely asymmetric. Combining $(V_T^s, V_R^s, w^s)$ in (A1a) and (A2) with $(V_T^a, V_R^a, w^a)$ in (A4) gives the 3D velocity of VF, that is, $(V_R, V_T, w') \equiv (V_R^s + V_R^a, V_T^s + V_T^a, w^s + w^a)$ in $(R, \beta, z')$. Using the coordinate transformation in (2.4) of Part I, this VF can be expressed by

$$(u', v', w') = (V_R\cos\beta - V_T\sin\beta, V_R\sin\beta + V_T\cos\beta, w') \quad \text{in } (x', y', z'). \tag{2.1}$$

As explained in appendix A, the two parts of the VF formulated in (A1)–(A4) satisfy the mass continuity equation [see (2.3) of Part I] and the two boundary conditions at $z' = 0$ and $R = 0$, and so does their combined VF field in (2.1).

The vector field of $(u', v')$ and the scalar field of $w'$ in (2.1) are plotted for the benchmark VF by the black arrows and blue contours, respectively, at $z' = 1$ km in Fig. 1b and at $z' = 4$ km in Fig. 1c. As shown by the black arrows in these two figures, the horizontal velocity is mainly along the tangential direction and its horizontal distribution is close to axisymmetric especially in and around the vortex core (i.e., the circular area of $R \le R_1$, where $R_1$ is the radius of maximum $V_T^s$). The horizontal flow is thus dominated by the axisymmetric tangential velocity $V_T^s$ and its vertical variation is also dominated by the vertical variation of $V_T^s$ governed by $1 + 0.5\tanh(z'/h)$.

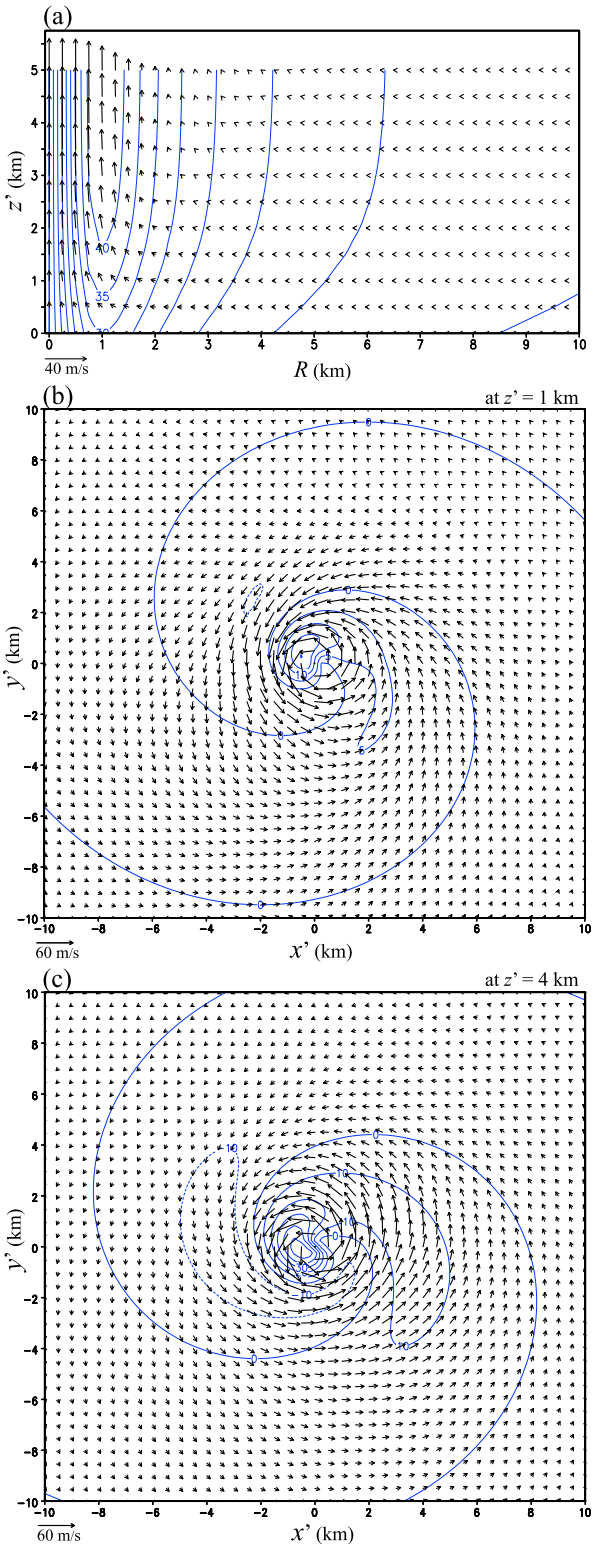


FIG. 1. (a) Benchmark $V_T^s$ and $(V_R^s, w^s)$ plotted in $(R, z')$ by blue contours (every 5 m s$^{-1}$) and black arrows, respectively. (b) Benchmark $(u', v')$ and $w'$ formulated in (2.4) plotted by black arrows and blue contours, respectively, at $z' = 1$ km. (c) As in (b), but at $z' = 4$ km. The vector scale is shown below the lower-left corner of each panel. The contours of $w'$ are plotted every 5 m s$^{-1}$ in (b), but every 10 m s$^{-1}$ in (c).

The blue contours in Figs. 1b and 1c show that the horizontal distribution of $w'$ is not close to axisymmetric even within the vortex core and becomes increasingly nonaxisymmetric as $R$ increases beyond the vortex core. In particular, the two spiral bands of positive and negative $w'$ outside the vortex core are distinctly nonaxisymmetric and is thus dominated by $w^a$—the asymmetric part of $w'$ formulated in (A4c). According to (A3a) and (A4c), the horizontal distribution of $w^a$ is featured by a pair of spiral bands of positive and negative $w^a$ winding around and toward the vortex center from two opposite directions at each vertical level above the ground. As the vertical level increases from $z' = 0$ to $D = 5$ km, the two paired spiral bands of $w^a$ become increasingly strong [because their amplitudes increase with $z'$ in proportion to $\tanh(z'/h)/\rho_a$] and their overall patterns rotate around the vortex center cyclonically by $\pi/2$ (=90°). Since $w'$ is dominated by $w^a$ outside the vortex core, the above described structures of $w^a$ also largely describe the structures of $w'$ outside the vortex core especially in the middle and upper levels of the analysis domain as shown by the blue contours in Fig. 1c.

Note that the density-weighted vertically integrated velocity-potential $X$ formulated in (A3a) and the density-weighted streamfunction $Y$ formulated in (A3b) have the same horizontal distributions but with opposite signs. Note also that the slantwise-vertical velocity for the asymmetric part of VF is related to $X$ by $w^a = -(\partial_x'^2 + \partial_y'^2)Y/\rho_a = -(\partial_R^2 + R^{-1}\partial_R + R^{-2}\partial\beta^2)X/\rho_a$ as shown in (A4c) and the slantwise-vertical vorticity for the asymmetric part of VF is defined by $\zeta^a \equiv (\partial_x'^2 + \partial_y'^2)Y/\rho_a = (\partial_R^2 + R^{-1}\partial_R + R^{-2}\partial\beta^2)Y/\rho_a$. The above relationships imply that the horizontal distribution of $\zeta^a$ is also featured by a pair of spiral bands with opposite signs, and the spiral band of positive (or negative) $\zeta^a$ is collocated with the spiral band of positive (or negative) $w^a$ at each vertical level above the ground. However, as implied by the formulation of $Y$ in (A3b), the amplitudes of the two paired spiral bands of $\zeta^a$ decrease with $z'$ in proportion to $\cosh(z'/h)^{-2}/\rho_a$. Thus, as the vertical level increases from $z' = 0$ to $D = 5$ km, the two paired spiral bands of $\zeta^a$ become weak but their overall patterns still rotate around the vortex center cyclonically by $\pi/2$ (=90°). The above described structures of $\zeta^a$ in connection with $w^a$ are not shown explicitly but they are embedded implicitly and subtly in the vector field of $(u', v')$ plotted by the black arrows in Figs. 1b and 1c. The coupled spiral bands of $w^a$ and $\zeta^a$ and their rotations with height are configured to resemble some asymmetric flow structures in observed tornadic mesocyclones (Marquis et al. 2012) so the benchmark VF can have adequate complexities for testing the VF-Var.

### b. *Simulated radial-velocity observations*

Using the coordinate transformation and variable transformation in (2.1)–(2.2) of Part I, the 3D velocity of the VF in (2.1) can be transformed to the total 3D velocity expressed by

$$(u, v, w) = \left(u' + w'\partial_z x_c + u_c, v' + w'\partial_z y_c + v_c, w'\right) \text{ in } (x, y, z, t), \tag{2.2}$$

where $(x_c, y_c)$ is the vortex center location—a vector function of $(z, t)$, and $(u_c, v_c) \equiv \partial_t(x_c, y_c)$ is the horizontal moving velocity of the vortex center. By considering differently slanted coordinate systems $(x', y', z')$, differently slanted vortices can be generated in $(x, y, z, t)$ from (2.2). These vortices satisfy the mass continuity equation and the aforementioned boundary conditions at $z = 0$ and along the vortex center axis.

Combining the downward terminal velocity of hydrometeors, denoted by $w_T$ (<0), into the 3D velocity in (2.2) gives $(u, v, w + w_T)$. Each radial-velocity observation can be simulated by projecting $(u, v, w + w_T)$ onto the direction of the radar beam at the concerned observation point plus a random observation error, and this gives

$$v_r^o = (u\sin\varphi + v\cos\varphi)\cos\theta + (w + w_T)\sin\theta + \varepsilon, \tag{2.3}$$

where $\varphi$ is the azimuthal angle (clockwise with respect to $y$ coordinate pointing to the north) of the observation point viewed from the radar site, $\theta$ is the slope angle of radar beam relative to the Earth surface beneath the observation point, and $\varepsilon$ denotes the random observation error (with a standard deviation of $\sigma_o = 1\ \text{m s}^{-1}$). Substituting (2.3) into (2.5) of Part I gives

$$\begin{aligned} v_r^i &= v_r^o - w_T\sin\theta - (u_c\sin\varphi + v_c\cos\varphi)\cos\theta \\ &= (u_v\sin\varphi + v_v\cos\varphi)\cos\theta + w\sin\theta + \varepsilon, \end{aligned} \tag{2.4}$$

where $v_r^i$ is the radial-velocity innovation and $(u_v, v_v) \equiv (u - u_c, v - v_c) = (u' + w'\partial_z x_c, v' + w'\partial_z y_c)$ are the two horizontal velocity components of VF in $(x, y, z)$ as shown in Table 1 of Part I.

Using (2.4), radial-velocity innovations are generated in the analysis domain by applying idealized Doppler scans and pseudo-operational Doppler scans to an upright (or eastward-slanted) vortex formulated by setting $u_c = 10\ \text{m s}^{-1}$ and $v_c = 0$ in (2.2) with $\partial_z x_c = \partial_z y_c = 0$ (or $\partial_z x_c = 0.5$ and $\partial_z y_c = 0$). The analysis domain is centered at $(x', y') = (0, 0)$ along the $z'$ coordinate (from $z' = 0$ to 5 km) and covers a square area of $20 \times 20\ \text{km}^2$ at each vertical level. The idealized Doppler scans are purely horizontal and unidirectional in parallel along horizontal grid lines of a coarse-resolution grid with $\Delta x' = \Delta y' = 0.5$ km at 5 vertical levels, every $\Delta z' = 1$ km, from $z' = 1$ to 5 km. In this case, radial-velocity observations and innovations are generated by setting $\theta = 0°$ and $\varphi = 270°$ (or 0°) in (2.3) and (2.4), respectively, on the coarse-resolution grid in the analysis domain. In this case, $v_r^o$ scanned from the east (or south) with $\varphi = 270°$ (or 0°) is simply $-u^o$ (or $v^o$) and the associated $v_r^o$ is simply $-u^i$ (or $v^i$). The pseudo-operational Doppler scans mimics the scan mode VCP12 used by operational WSR-88Ds for severe storms. In this mode, a full volume of radial velocity is scanned from each radar on 14 sweeps (at 0.5°, 0.9°, 1.3°, 1.8°, 2.4°, 3.1°, 4.0°, 5.1°, 6.4°, 8.0°, 10.0°, 12.5°, 15.6°, and 19.5°) over the analysis time window from $t = 0$ to 5 min, while the range resolution is 250 m and the azimuthal beam spacing is 0.5°. The first radar, called radar A (or the second radar, called radar B) is 30 km to the east (or south) of the vortex center on the ground ($z = 0$) at $t = 0$. Figure 2 shows the positions of radar A and radar B relative to the vortex-following moving analysis domain at the starting time ($t = 0$) and ending time ($t = 5$ min) of the analysis time window.

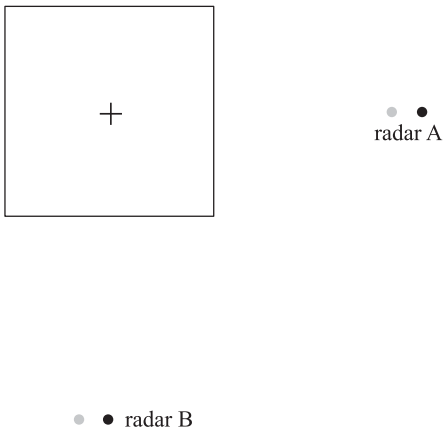


FIG. 2. Positions of radar A and radar B relative to the analysis domain at the starting and ending times of the analysis time window. The square box shows the $20 \times 20\,\text{km}^2$ area of vortex-following analysis domain on the ground level. The plus sign at the center of the square box shows the analysis domain center (also the vortex center) that is moving eastward toward radar A at the speed of $10\,\text{m s}^{-1}$. The black dot labeled with "radar A" (or "radar B") shows the position of radar A (or radar B), which is 30 km to the east (or south) of the vortex center on the ground ($z = 0$) at the starting time ($t = 0$), while the nearby gray dot to the west of the black dot shows the position of radar A (or radar B) at the ending time ($t = 5$ min) of the analysis time window.

## 3. Background error covariance parameter settings and experiment design

### a. *Parameter settings for background error covariance functions*

As explained in section 2c of Part I, for the stand-alone applications considered in this paper, the background wind is zero in $(x', y', z')$ so the background wind error is simply the true value of $(u', v', w')$ in $(x', y', z')$. For the axisymmetric part of benchmark VF shown in Fig. 1a, $V_T^s$ formulated in (A1a) has narrower structures than $V_R^s = -\partial_z' \psi^s/\rho_a$ formulated in (A2a), so the background error of $V_T^s$ tends to have narrower correlation structures than the background error of $\psi^s$. Based on this consideration, the background error decorrelation length factored into $r$ in (3.6) of Part I is set to $l = l_1 = 1/2$ for $V_T^s$ but set to $l = l_2 = 1$ for $\psi^s$, while $R_c = 1.5$ km is used for the coordinate transformation from $R$ to $r$ in (3.6) of Part I. The background error decorrelation depth factored into $h$ is set to $H = H_1 = H_2 = 2$ km for $V_T^s$ and $\psi^s$. Note that the vertical resolution of radial-velocity observations from the idealized (or pseudo-operational) Doppler scans is $\Delta z' = 1$ km (or coarser than 1 km in upper levels of the analysis domain), so spurious vertical variations can be generated in analyzed VFs if the background error decorrelation depth reduces (from 2 km) to 1 km. This explains why we set $H = H_1 = H_2 = 2$ km more or less empirically. When the decorrelation length $l$ in $r$ is transformed into the physical radial coordinate $R$, the decorrelation length in $R$ is a function of $R$ given by $L = R_c \sinh[(rl + l/2)] - R_c \sinh[(rl - l/2)] = 2R_c \cosh(rl) \sinh(l/2) = 2(R^2 + R_c^2)^{1/2} \sinh(l/2)$. For the above settings of $l = l_1 = 1/2$ and $l = l_2 = 1$, the corresponding values of $L$ at $R = R_c$ are $L_1 \approx R_c/\sqrt{2} \approx 1$ km and $L_2 \approx \sqrt{2}R_c \approx 2$ km, respectively.

The root-mean-square values of benchmark $V_T^s$ and $V_R^s$ within 5 km from the vortex center in the analysis domain are 20.7 and $1.9\,\text{m s}^{-1}$, respectively, so the background error standard deviation can be set to $\sigma_1 = 20\,\text{m s}^{-1}$ for $V_T^s$ and to $\sigma_R = 2\,\text{m s}^{-1}$ for $V_R^s$. Note that $V_R^s \equiv -\partial_{z'}\psi^s/\rho_a = -\partial_h \psi^s/\rho_a H_2$ according to (2.3) and (3.6) of Part I. Applying this relationship to the background error covariance formulated for $\psi^s$ in (3.8b) of Part I gives the background error covariance of $V_R^s$ in the following form:

$$\begin{aligned}\left(\partial_{z_i'}\partial_{z_j'}B_{2ij}\right)\Big/\rho_i\rho_j &= \sigma_2^2\left[\left(d_z\ln\rho_a\right)_i\left(d_z\ln\rho_a\right)_j G_0\left(r_i,r_j\right)G_0\left(h_i,h_j\right) + G_0\left(r_i,r_j\right)\partial_{hi}\partial_{hj}G_0\left(h_i,h_j\right)\Big/H_2^2\right]\\ &\approx \sigma_2^2 G_0\left(r_i,r_j\right)\partial_{hi}\partial_{hj}G_0\left(h_i,h_j\right)\Big/H_2^2\\ &= \sigma_2^2 G_0\left(r_i,r_j\right)\left\{\left[1-\left(h_i-h_j\right)^2\right]G\left(h_i-h_j\right) + \left[1-\left(h_i+h_j\right)^2\right]G\left(h_i+h_j\right)\right\}\Big/H_2^2. \end{aligned} \tag{3.1}$$

For $i = j$, (3.1) gives the background error variance of $V_R^s$ as a function of $(r_i, h_i)$ in the following form:

$$\sigma_R^2 \approx \sigma_2^2 \frac{\left[1 - G(2r_i)\right]\left[1 + \left(1 - 4h_i^2\right)G(2h_i)\right]}{H_2^2}. \tag{3.2}$$

For $r_i \geq 1$ and $h_i \geq 0.5$, (3.2) gives $\sigma_2 \approx \sigma_R H_2$. Thus, in summary, we can set $\sigma_1 = 20\,\text{m s}^{-1}$ with $l = l_1 = 1/2$ and $H = H_1 = 2$ km for the background error covariance function formulated for $V_T^s$ in (3.8a) of Part I, and set $\sigma_2 = \sigma_R H_2$ with $\sigma_R = 2\,\text{m s}^{-1}$, $H = H_2 = 2$ km and $l = l_2 = 1$ for the background error covariance function formulated for $\psi^s$ in (3.8b) of Part I.

For the asymmetric part, the background error decorrelation length factored into $r$ is set to $l = l_3 = 1$ for $X$ but to $l = l_4 = 1/\sqrt{2}$ for $Y$, while the background error decorrelation depth factored into $h$ is set to $H = H_3 = \sqrt{3}$ (=1.732) km for $X$ but set to $H = H_4 = 2$ km for $Y$. These settings of $l$ and $H$ are selected loosely by considering that the rotational velocity field associated with $Y$ tends to have narrower and deeper structures than the divergent velocity field associated with $X$. For the above settings of $l = l_3 = 1$ and $l = l_4 = 1/\sqrt{2}$, the corresponding values of $L$ at $R = R_c$ are $L_3 \approx \sqrt{2}R_c \approx 2$ km and $L_4 \approx R_c = 1.5$ km, respectively.

The root-mean-square values of the divergent (or rotational) part of benchmark $(u^a, v^a)$ computed from $X$ (or $Y$) within 5 km from the vortex center in the analysis domain is 4.9 (or 3.2) $\text{m s}^{-1}$, so the background error standard deviation can be set to $\sigma_d = 5$ (or $\sigma_r = 3$) $\text{m s}^{-1}$ for the divergent (or rotational) part of $(u^a, v^a)$. The background error standard deviation for $\partial_{z'}X$ (or $Y$) can be

then estimated by $\sigma_d L_3/\sqrt{2}$ (or $\sigma_r L_4/\sqrt{2}$) according to (A13)–(A.14) of Xu et al. (2010), and the background error standard deviation for $X$ can be finally estimated by $\sigma_d L_3 H_3/\sqrt{2}$ by using the relationship derived similarly to that in (3.1)–(3.2). Thus, in summary, we set $\sigma_3 = \sigma_d L_3 H_3/\sqrt{2}$ with $\sigma_d = 5\,\mathrm{m\,s^{-1}}$, $L_3 = 2\,\mathrm{km}$, $l = l_3 = 1$ and $H = H_3 = \sqrt{3}(=1.732)\,\mathrm{km}$ for the background error covariance function formulated for $X$ in (4.8a) of Part I, and set $\sigma_4 = \sigma_r L_4/\sqrt{2}$ with $\sigma_r = 3\,\mathrm{m\,s^{-1}}$, $L_4 = 1.5\,\mathrm{km}$, $l = l_4 = 1/\sqrt{2}$, $H = H_4 = 2\,\mathrm{km}$ for the background error covariance function formulated for $Y$ in (4.8b) of Part I. For the decorrelation arc defined by $\Phi \equiv 2\sinh(l/2) + [\Phi_0 - 2\sinh(l/2)]R_p/(R + R_p)$ in (4.9) of Part I, we set $\Phi_0 = \pi/2$ and $R_p = 5\,\mathrm{km}$. The above parameter settings are used for all the experiments designed in the next subsections.

### b. Experiment design

The aforementioned upright and slanted vortices are assumed to be stationary in the moving coordinate system ($x'$, $y'$, $z'$) within the analysis time window, so the location of radar A (or radar B) changes with time in ($x'$, $y'$, $z'$) and this affects the calculations of $\varphi$ and $\theta$ at each observation point for the pseudo-operational Doppler scans (but not the idealized Doppler scans). Radial velocities scanned on the two highest sweeps at 15.6° and 19.5° from either radar A or B are located above the analysis domain and thus not used for the analyses, so only 12 sweeps are used. These 12 sweeps are scanned sequentially from each radar every $\Delta t = 20\,\mathrm{s}$ from $t = 0$ (at 0.5°) to $240\,\mathrm{s} = 4\,\mathrm{min}$ (at 12.5°). When the radial-velocity observations (generated in each radar coordinate system) are transformed into the moving coordinate system ($x'$, $y'$, $z'$), the location of each radar is fixed and calculated for each sweep at the beginning time of the sweep, so the small time differences between azimuthal scans on the same sweep are neglected.

For each type of Doppler scans, experiments are designed in three pairs to test the VF-Var by applying the two-step analysis versus the single-step analysis to three innovation datasets. For the idealized Doppler scans, the three innovation datasets are (i) the dual-Doppler innovations given by $(-u^i, v^i)$, (ii) the single-Doppler innovations given by $-u^i$ only, and (iii) the single-Doppler innovations given by $v^i$ only. The three experiments performed by applying the two-step analysis (or single-step analysis) to these three datasets are named E-uv-2, E-u-2, and E-v-2 (or E-uv-1, E-u-1, and E-v-1), respectively. The results of these experiments tested with the upright and slanted vortices will be presented and examined in sections 4a and 4b, respectively. For the pseudo-operational Doppler scans, the three innovation datasets are (i) the dual-Doppler innovations from radar A and radar B, (ii) the single-Doppler innovations from radar A only, and (iii) the single-Doppler innovations from radar B only. The three experiments performed by applying the two-step analysis (or single-step analysis) to these three datasets are named E-AB-2, E-A-2, and E-B-2 (or E-AB-1, E-A-1, and E-B-1), respectively. The results of these experiments tested with the upright and slanted vortices will be presented and examined in sections 5a and 5b, respectively.

As explained at the end of section 4 of Part I, the analyzed VF is a spatially continuous vector field. The benchmark VF formulated in (A2) and (A4) is also a continuous vector field, so the performance of VF-Var can be evaluated on any high-resolution grid. However, the intrinsic spatial resolution of the analyzed VF is limited by the length scale resolvable by the background error correlation functions in connection with spatial distributions of observations. Based on this consideration, the horizontal (or vertical) grid resolution used for evaluating the performance of VF-Var is set to $\Delta x' = \Delta y' = 0.25\,\mathrm{km}$ (or $\Delta z' = 0.5\,\mathrm{km}$) which is finer than the smallest background error decorrelation length (or depth) and roughly matches the highest horizontal (or vertical) resolution of non-uniformly distributed observations from the pseudo-operational Doppler scans. This evaluation grid (with $\Delta x' = \Delta y' = 0.25\,\mathrm{km}$ and $\Delta z' = 0.5\,\mathrm{km}$) will be used in the next two sections to calculate the cylindrical-volume-averaged RMS error (CRE) for each analyzed field centered at $(x', y') = (0, 0)$ within $R \le 5\,\mathrm{km}$ through the entire depth (from $z' = 0$ to 5 km) of the analysis domain as well as the domain-averaged RMS error (DRE) over the entire analysis domain.

TABLE 1. Cylindrical-volume-averaged RMS errors (CREs) of analyzed ($V_T^s$, $V_R^s$, $w^s$) and diagnosed ($V_T^{s+}$, $V_R^{s+}$, $w^{s+}$) from experiments performed with idealized Doppler scans of upright vortex in section 4a. The cylindrical-volume average is taken over the volume within $R \le 5\,\mathrm{km}$ through the entire depth (from $z' = 0$ to 5 km) of the analysis domain. As described in section 3b, each experiment is named in three parts. The letter "uv," "u," or "v" in the middle part means that the experiment is performed with the dual-Doppler innovations given by $(-u^i, v^i)$, the single-Doppler innovations given by $-u^i$ only, or the single-Doppler innovations given by $v^i$ only. The number "1" (or "2") in the last part means that the experiment is performed by applying the two-step analysis (or single-step analysis).

| Expt | $V_T^s$ | $V_R^s$ | $w^s$ | $V_T^{s+}$ | $V_R^{s+}$ | $w^{s+}$ |
|---|---|---|---|---|---|---|
| E-uv-2 | 0.194 | 0.163 | 0.695 | 0.188 | 0.138 | 0.460 |
| E-uv-1 | 0.215 | 0.664 | 2.412 | 0.185 | 0.137 | 0.486 |
| E-u-2 | 0.260 | 0.188 | 0.705 | 0.266 | 0.186 | 0.546 |
| E-u-1 | 0.293 | 0.624 | 2.246 | 0.269 | 0.188 | 0.517 |
| E-v-2 | 0.244 | 0.216 | 0.944 | 0.270 | 0.138 | 0.494 |
| E-v-1 | 0.278 | 0.836 | 2.877 | 0.260 | 0.230 | 0.791 |

## 4. Experiments with idealized Doppler scans

### a. Results for upright vortex

For the experiments performed with idealized Doppler scans of the upright vortex, the CRE is listed for each analyzed field of ($V_T^s$, $V_R^s$, $w^s$) in Table 1 and each analyzed field of ($u'$, $v'$, $w'$) in Table 2. As shown in row 1 of Table 1 for the two-step analysis in E-uv-2, the CREs of analyzed ($V_T^s$, $V_R^s$) are much smaller than the observation error standard deviation $\sigma_o$ ($=1\,\mathrm{m\,s^{-1}}$) and the CRE of analyzed $w^s$ is also smaller than $\sigma_o$, so the axisymmetric part of VF is analyzed very accurately. The CREs of analyzed ($u'$, $v'$) in E-uv-2 are also smaller than $\sigma_o$ (see row 1 of Table 2) as they should be because $u$ and $v$ are observed. However, the CRE of analyzed $w'$ is larger than $\sigma_o$. This is expected because $w'$ is not observed and has complex structures. Thus, the total VF is also well analyzed in E-uv-2 although the relative CRE (RCRE) of analyzed $w'$ is as large as 30.2%. On the other hand, the CREs of analyzed ($V_T^s$, $V_R^s$) from the single-step analysis in E-uv-1 are larger than those

TABLE 2. As in Table 1, but for CREs and RCREs of analyzed $(u', v', w')$, where RCRE stands for relative CRE defined by the ratio of CRE with respect to the cylindrical-volume-averaged RMS value of the related benchmark field.

| | CRE (m s$^{-1}$) | | | RCRE (%) | | |
|---|---|---|---|---|---|---|
| Expt | $u'$ | $v'$ | $w'$ | $u'$ | $v'$ | $w'$ |
| E-uv-2 | 0.744 | 0.612 | 2.838 | 4.9 | 4.0 | 30.2 |
| E-uv-1 | 0.747 | 0.619 | 2.908 | 4.9 | 4.1 | 30.9 |
| E-u-2 | 0.717 | 2.243 | 3.101 | 4.7 | 14.7 | 33.0 |
| E-u-1 | 0.719 | 2.247 | 3.116 | 4.8 | 14.8 | 33.1 |
| E-v-2 | 3.932 | 0.576 | 3.440 | 26.0 | 3.8 | 36.6 |
| E-v-1 | 3.936 | 0.571 | 3.502 | 26.0 | 3.7 | 37.2 |

from the two-step analysis in E-uv-2 (see row 1 vs row 2 of Table 1) but still smaller than $\sigma_o$, whereas the CRE of analyzed $w^s$ in E-uv-1 becomes much larger than $\sigma_o$. However, the CREs of analyzed $(u', v', w')$ in E-uv-1 (see row 2 of Table 2) are only slightly larger than those from E-uv-2 (see row 1 of Table 2) and so are their associated RCREs. Thus, in this case, the two-step analysis outperforms the single-step analysis especially in analyzing the axisymmetric part of VF.

As explained in appendix A, the fields of $(V_T^a, V_R^a, w^a)$ formulated in (A4) for the asymmetric part of benchmark VF are purely asymmetric. However, the analyzed $(V_T^a, V_R^a, w^a)$ are not purely asymmetric, so the total axisymmetric part of VF should be diagnosed by $(V_T^{s+}, V_R^{s+}, w^{s+}) \equiv (V_T^s, V_R^s, w^s) + (2\pi)^{-1}\int_{-\pi}^{\pi}(V_T^a, V_R^a, w^a)\,d\beta$. The CREs of diagnosed $(V_T^{s+}, V_R^{s+}, w^{s+})$ are listed in the last three columns of Table 1. As shown in row 1 (or row 2) of Table 1, the diagnosed $(V_T^{s+}, V_R^{s+}, w^{s+})$ are slightly (or substantially) more accurate than the directly analyzed $(V_T^s, V_R^s, w^s)$ in E-uv-2 (or E-uv-1), whereas the diagnosed $(V_T^{s+}, V_R^{s+}, w^{s+})$ in E-uv-1 are as accurate as those in E-uv-2.

When dual-Doppler innovations $(-u^i, v^i)$ reduce to single-Doppler innovations $-u^i$, the analyzed $(V_T^s, V_R^s, w^s)$ and diagnosed $(V_T^{s+}, V_R^{s+}, w^{s+})$ become slightly less accurate (as seen from row 3 vs row 1 in Table 1), the analyzed $u'$ (or $w'$) become slightly less (or more) accurate but the analyzed $v'$ becomes much less accurate (as seen from row 3 vs row 1 in Table 2). The reduced accuracy in $v'$ is apparently caused by the absence of $v^i$ in the single-Doppler innovations. On the other hand, as shown in row 4 of Table 1 for the single-step analysis applied to $-u^i$ in E-u-1, the CREs of analyzed $(V_T^s, V_R^s)$ are larger than those from the two-step analysis in E-u-2 (see row 3 of Table 1) but still smaller than $\sigma_o$ whereas the CRE of analyzed $w^s$ becomes larger than $\sigma_o$. In this case, the diagnosed $V_T^{s+}$ (or $V_R^{s+}$) is slightly (or substantially) more accurate than the analyzed $V_T^s$ (or $V_R^s$) and the diagnosed $w^{s+}$ is much more accurate than the analyzed $w^s$. Thus, the axisymmetric part of VF is not well analyzed directly but well diagnosed indirectly in E-u-1. As shown in row 4 versus row 3 of Table 2, the CREs of analyzed $(u', v', w')$ in E-u-1 are nearly the same as those from E-u-2 and so are their associated RCREs.

For the two-step analysis applied to $v^i$ in E-v-2, the CREs of analyzed $(V_T^s, V_R^s, w^s)$ and diagnosed $(V_T^{s+}, V_R^{s+}, w^+)$ in row 5 of Table 1 are comparable to those from E-u-2 in row 3 of Table 1, and the CREs of analyzed $u'$ and $(v', w')$ in row 5 of Table 2 are comparable to those of analyzed $v'$ and $(u', w')$ from E-u-2 in row 3 of Table 2. The increased CRE of analyzed $u'$ in E-v-2 is similar to the increased CRE of analyzed $v'$ in E-u-2 but is now caused by the absence of $u^i$ in the single-Doppler innovations. For the single-step analysis applied to $-v^i$ in E-v-1, the CREs of analyzed $(V_T^s, V_R^s, w^s)$ and diagnosed $(V_R^{s+}, w^+)$ (or $V_T^{s+}$) in row 6 of Table 1 are larger (or slightly smaller) than those from the two-step analysis in E-v-2 (see row 5 of Table 1), but the CREs of analyzed $(u', v', w')$ in row 6 of Table 2 are nearly the same as those from the two-step analysis in E-u-2 (see row 5 of Table 2) and so are their associated RCREs.

DREs of analyzed $(u', v', w')$ are also computed (on a grid with $\Delta x' = \Delta y' = 0.25$ km and $\Delta z' = 0.5$ km) over the entire analysis domain (rather than within $R \le 5$ km). The computed DRE is roughly a half of CRE for each analyzed field of $(u', v', w')$ while the domain-averaged RMS value is also roughly a half of the cylindrical-volume-averaged RMS value for each benchmark field. Thus, the relative DRE (RDRE; defined by the ratio of DRE with respect to the domain-averaged RMS value of the related benchmark field) is roughly the same as the RCRE listed in Table 2 for each analyzed field of $(u', v', w')$ in each experiment. For each analyzed field of $(u', v', w')$, the DRE is a vertical average of the area-averaged RMS error (ARE), and the ARE is calculated (on a grid with $\Delta x' = \Delta y' = 0.25$ km) over the entire area of the analysis domain at each vertical level. The AREs of analyzed $(u', v', w')$ from the above three pairs of experiments are shown as functions of $z'$ in Figs. 3a–c. As shown, the AREs of single-step analyzed $(u', v', w')$ have nearly the same vertical distributions as those of their respective two-step analyzed $(u', v', w')$. As shown by the red (or green) dashed curve in Fig. 3b (or Fig. 3c), the ARE of analyzed $u'$ (or $v'$) in E-u-2 (or E-v-2) is similar to that from E-uv-2 shown in Fig. 3a, which is nearly constant (around $\sigma_o/4$) for $z' \ge 1$ km but increases nearly 4 times (to about $\sigma_o = 1$ m s$^{-1}$) as $z'$ decreases from 1 to 0 km. This increase of ARE is due to the absence of observation below $z' = 1$ km. On the other hand, the ARE of analyzed $v'$ (or $u'$) in E-u-2 (or E-v-2) is substantially larger than that from E-uv-2 shown in Fig. 3a, and this increase of ARE is due to the absence of $v^i$ (or $u^i$) in the single-Doppler innovations as explained earlier. However, the absence of $v^i$ (or $u^i$) causes only a moderate increase of ARE for the analyzed $w'$ in E-u-2 (or E-v-2) from that in E-uv-2. Note that the analyzed $w'$ is ensured to satisfy the boundary condition of $w' = 0$ at $z' = 0$ (see section 4 of Part I) and the area-averaged RMS value of benchmark $w'$ increase with $z'$. This explains why the ARE of analyzed $w'$ is zero at $z' = 0$ and increases with $z'$ as shown by the blue curve for each experiment in Fig. 3.

The analyzed $V_T^s$ and $(V_R^s, w^s)$ in E-u-2 are shown in Fig. 4a against their respective benchmark fields. As shown, even with single-Doppler innovations, the analyzed $V_T^s$ and $(V_R^s, w^s)$ match their respective benchmark fields quite closely, which is consistent with their small CREs listed in row 3 of Table 1. The analyzed $(u', v')$ and $w'$ in E-u-2 are shown against their respective benchmark fields at $z' = 1$ km in Fig. 4b and $z' = 4$ km in Fig. 4c. As shown, the analyzed $(u', v')$ is very close to the benchmark field and the difference from the benchmark is

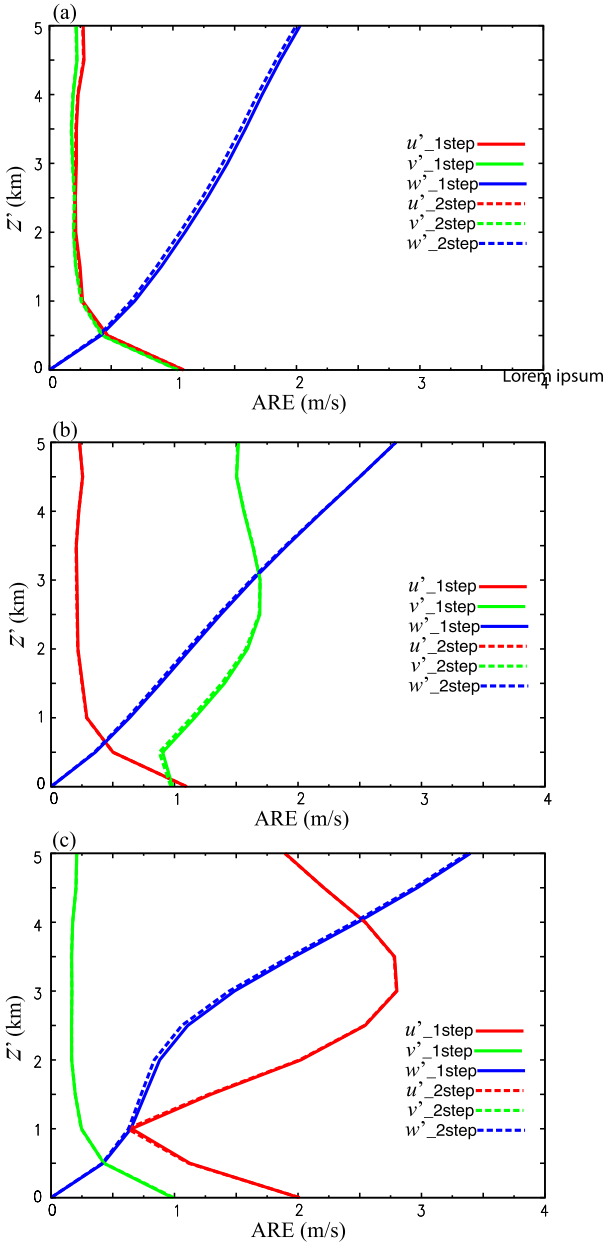


FIG. 3. Area-averaged RMS errors (AREs) plotted as functions of $z'$ for analyzed ($u'$, $v'$, $w'$) from three pairs of experiments performed with idealized Doppler scans of upright vortex: (a) E-uv-1 vs E-uv-2 for dual-Doppler analyses, (b) E-u-1 vs E-u-2 for single-Doppler analyses with $u$-component observations only, and (c) E-v-1 vs E-v-2 for single-Doppler analyses with $v$-component observations only. The area average is taken over the entire $20 \times 20\,\text{km}^2$ area of the analysis domain at each vertical level.

small ($<$ or $\ll 5\,\text{m s}^{-1}$) and mainly in the direction of unobserved $v$ component, while the analyzed $w'$ captures the dominant updraft and downdraft structures. However, largest errors are seen for the analyzed $w'$ inside the vortex core, especially in the upper levels. These large errors are caused by the rapid horizontal variations of $w'$ inside the vortex core that

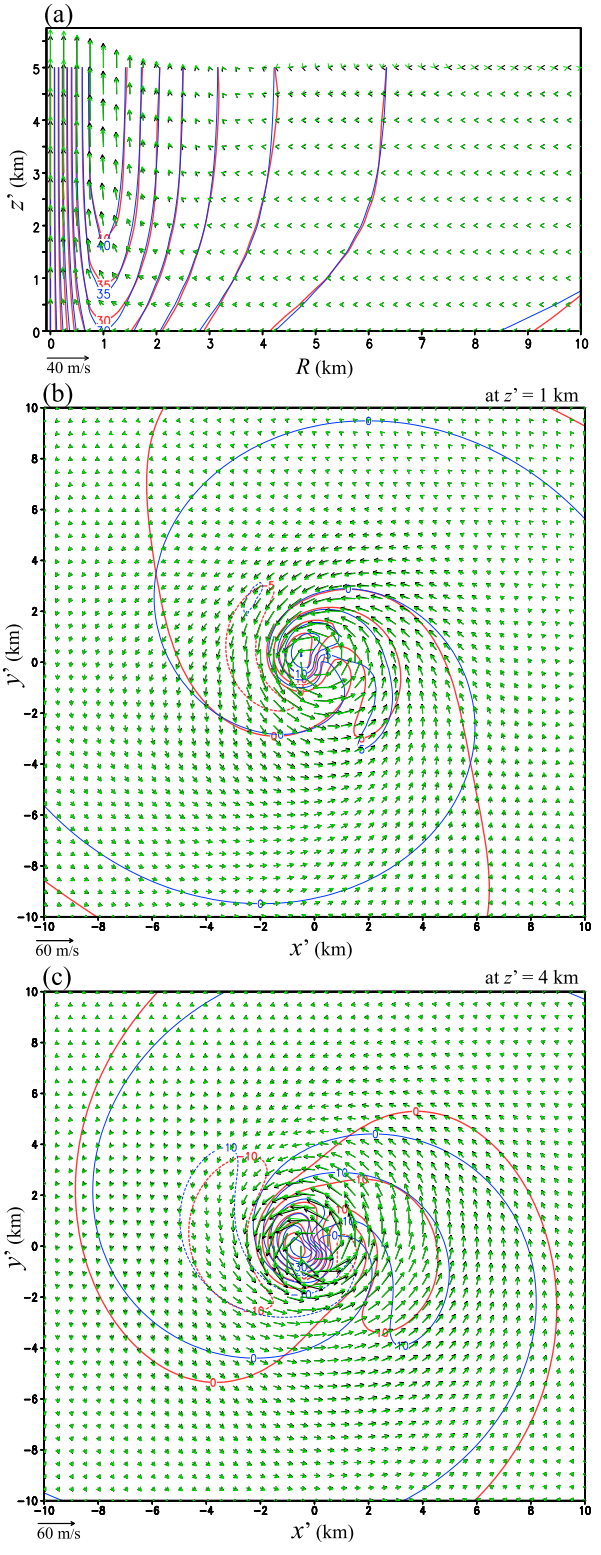


FIG. 4. (a) As in Fig. 1a, but overlapped by analyzed $V_T^s$ and $(V_R^s, w^s)$ from E-u-2 plotted by red contours and green arrows, respectively. (b),(c) As in Figs. 1b and 1c, but overlapped by analyzed $(u', v')$ and $w'$ from E-u-2 plotted by green arrows and red contours, respectively. E-u-2 is performed with idealized Doppler scans of upright vortex.

TABLE 3. As in Table 1, but from experiments performed with idealized Doppler scans of eastward-slanted vortex in section 4b.

| Expt | $V_T^s$ | $V_R^s$ | $w^s$ | $V_T^{s+}$ | $V_R^{s+}$ | $w^{s+}$ |
|---|---|---|---|---|---|---|
| E-uv-2 | 1.676 | 2.341 | 2.243 | 0.339 | 0.615 | 0.873 |
| E-uv-1 | 0.341 | 0.805 | 1.779 | 0.325 | 0.376 | 0.643 |
| E-u-2 | 3.325 | 3.854 | 3.004 | 2.247 | 1.000 | 1.088 |
| E-u-1 | 1.643 | 0.873 | 1.744 | 1.605 | 0.406 | 0.628 |
| E-v-2 | | | As in Table 1 | | | |
| E-v-1 | | | As in Table 1 | | | |

TABLE 4. As in Table 2, but from experiments performed with idealized Doppler scans of eastward-slanted vortex in section 4b.

| | CRE (m s$^{-1}$) | | | RCRE (%) | | |
|---|---|---|---|---|---|---|
| Expt | $u'$ | $v'$ | $w'$ | $u'$ | $v'$ | $w'$ |
| E-uv-2 | 0.836 | 0.690 | 1.590 | 5.5 | 4.5 | 16.9 |
| E-uv-1 | 0.747 | 0.596 | 1.420 | 4.9 | 3.9 | 15.1 |
| E-u-2 | 1.889 | 3.599 | 3.683 | 12.5 | 23.6 | 39.1 |
| E-u-1 | 1.414 | 2.544 | 2.683 | 9.3 | 16.7 | 28.5 |
| E-v-2 | | | As in Table 2 | | | |
| E-v-1 | | | As in Table 2 | | | |

cannot be well resolved by the VF-dependent background error correlation functions in connection with the very limited number of observations inside the vortex core. When the innovations are given by $(-u^i, v^i)$ instead of $-u^i$, the analyzed $(u', v')$ and $w'$ (not shown) become, as expected, much closer to their respective benchmark fields than those in Figs. 4b and 4c. Thus, when the vortex is upright, the two-step analysis performs very well with the idealized dual-Doppler innovations and reasonably well with the idealized single-Doppler innovations, whereas the single-step analysis underperforms the two-step analysis slightly in analyzing $(u', v', w')$ and substantially in analyzing $(V_T^s, V_R^s, w^s)$.

### b. Results for slantwise vortex

For the experiments performed with the eastward-slanted vortex [formulated by setting $\partial_z x_c = 0.5$ and $\partial_z y_c = 0$ in (2.2)–(2.4)], the resulting CREs are listed in Tables 3 and 4 . As shown in row 1 of Table 3 for the two-step analysis applied to $(-u^i, v^i)$ in E-uv-2, the CREs of analyzed $(V_T^s, V_R^s, w^s)$ become much larger and the CREs of diagnosed $(V_T^{s+}, V_R^{s+}, w^{s+})$ also become larger when compared to the upright vortex (see row 1 of Table 1) but the latter CREs are still smaller than $\sigma_o$. As shown in row 1 of Table 4, the CREs of analyzed $(u', v')$ are slightly larger but the CRE of analyzed $w'$ is substantially smaller when compared to the upright vortex (see row 1 of Table 2). Thus, when the vortex becomes slanted, the axisymmetric part of VF becomes difficult to analyze directly but still can be diagnosed indirectly with less reduced accuracies. In this case, the analyzed $(u', v')$ become slightly less accurate but the analyzed $w'$ becomes substantially more accurate for the two-step analysis in E-uv-2. On the other hand, as shown in row 2 of Table 3 for the single-step analysis applied to $(-u^i, v^i)$ in E-uv-1, the analyzed $(V_T^s, V_R^s, w^s)$ and diagnosed $(V_T^{s+}, V_R^{s+}, w^{s+})$ are more accurate than those from the two-step analysis in E-uv-2 (see row 1 of Table 3). Also, as seen by comparing row 2 with row 1 in Table 4, the analyzed $(u', v', w')$ in E-uv-1 are slightly more accurate than those from E-uv-2. Thus, the single-step analysis outperforms the two-step analysis in this case.

When only considering single-Doppler innovations with $(-u^i, v^i)$ reduced to $-u^i$, the analyzed $(V_T^s, V_R^s, w^s)$ and diagnosed $(V_T^{s+}, V_R^{s+}, w^{s+})$ become less accurate especially for the two-step analysis [as seen by comparing rows 3 with row 1 in Table 3] while the analyzed $(u', w')$ also become less accurate and the analyzed $v'$ becomes much less accurate [as seen by comparing row 3 (or row 4) with row 1 (or row 2) in Table 4]. In this case, the CREs in row 3 of Table 3 (or Table 4) for the two-step analysis are still larger than those from the single-step analysis shown in row 4 of Table 3 (or Table 4). Thus, when $(-u^i, v^i)$ reduce to $-u^i$, the axisymmetric part of VF and $(u', w')$ become more difficult to analyze, the analyzed $v'$ becomes much less accurate (due again to the absence of $v^i$ in the single-Doppler innovations), and the single-step analysis still outperforms the two-step analysis.

When only considering single-Doppler innovations with $(-u^i, v^i)$ reduced to $v^i$, the innovations $v^i$ used in E-v-2 and E-v-1 are not affected by the vortex eastward slanting because $v^i$ is given by $v' + \varepsilon$ for $\theta = 0°$ and $\varphi = 0°$ with $\partial_z y_c = 0$ in (2.4) although $\partial_z x_c = 0.5 \neq 0$. In this case, the innovations $v^i$ remain the same as those used in section 4a for the upright vortex with $\partial_z x_c = \partial_z y_c = 0$ except that they are now located in the slantwise coordinates $(x', y', z')$ with $\partial_z x_c = 0.5$. This explains why the CREs in rows 5 and 6 of Table 3 (or Table 4) are the same as those for the upright vortex shown in row 5 and 6 of Table 1 (or Table 2), respectively.

On the other hand, $-u^i$ is given by $-(u' + w'\partial_z x_c + \varepsilon)$ for $\theta = 0°$ and $\varphi = 270°$ with $\partial_z x_c = 0.5$ in (2.4) and thus contains a projection of the slantwise vertical velocity $w'$. When the VF is expressed by $(u', v', w')$ in terms of the covariant basis vectors in $(x', y', z')$, $w'\partial_z x_c$ is not a part of $u'$ and thus can be partitioned into $w^s\partial_z x_c$ and $w^a\partial_z x_c$. However, when the VF is expressed by $(u_v, v_v, w)$ in (2.4) and observed in $(x, y, z)$, $w'\partial_z x_c$ becomes a part of $u_v$, so $w^s\partial_z x_c$ (or $w^a\partial_z x_c$) is no longer purely axisymmetric (or asymmetric) as a part of $(u_v, v_v)$. For this reason, as explained in section 2b of Part I, the VF cannot be analyzed in a properly partitioned form by a 2DVar at a given vertical level unless $\partial_z x_c = \partial_z y_c = 0$. For the same reason, when the axisymmetric part of VF is analyzed alone in the first step in E-uv-2 or E-u-2, the attribution of $w^s\partial_z x_c$ (or $w^a\partial_z x_c$) to the asymmetric (or axisymmetric) part of $(u_v, v_v)$ is not counted. This explains why the analyzed $(V_T^s, V_R^s, w^s)$ in E-uv-2 and E-u-2 become less accurate as the vortex becomes slanted eastward (with $\partial_z x_c$ increased from 0 to 0.5). On the other hand, when the axisymmetric part is analyzed jointly with the asymmetric part in E-uv-1 (or E-u-1), the attributions of $w^s\partial_z x_c$ and $w^a\partial_z x_c$ to the asymmetric and axisymmetric parts of $(u_v, v_v)$ are all counted. This explains why $(V_T^s, V_R^s, w^s)$ are analyzed more accurately in E-uv-1 (or E-u-1) than in E-uv-2 (or E-u-2). Besides, since the analyzed $(u^a, v^a, w^a)$ diminish rapidly toward the vortex center in the vortex core (see appendix C of Part I), errors in $(V_T^s, V_R^s, w^s)$ produced in the first-step analysis cannot be corrected (or corrected effectively) at (or around) the

vortex center by the second-step analysis in E-uv-2 or E-u-2. This explains why the diagnosed $(V_T^{s+}, V_R^{s+}, w^{s+})$ in E-uv-2 (or E-u-2) are still less accurate than those from the single-step analysis in E-uv-1 (or E-u-1). Furthermore, by noting that $w'$ is a part of $-u^i = -(u' + w'\partial_z x_c + \varepsilon)$ and thus is partially observed for $\partial_z x_c = 0.5$, one can see why $w'$ is analyzed more accurately in E-uv-2 (or E-uv-1) when the vortex becomes slanted eastward [as seen by comparing row 1 (or row 2) in Table 4 with that in Table 2].

The AREs of analyzed $(u', v', w')$ from the above two pairs of experiments are shown as functions of $z'$ in Figs. 5a and 5b. As shown, the single-step analyzed $(u', v', w')$ are more accurate than their respective two-step analyzed $(u', v', w')$, and the analyzed $u'$ (or $v$) in E-u-1 or E-u-2 is less (or much less) accurate than that in E-uv-1 or E-uv-2. These comparisons are consistent with the results in Table 4. In addition, as shown by the solid curves in Fig. 5 versus those in Fig. 3, when the vortex becomes slanted eastward, the dual-Doppler analyzed $u'$ (or $w'$) in E-uv-1 becomes less (or more) accurate and the single-Doppler analyzed $u'$ (or $w'$) in E-u-1 becomes substantially less (or slightly more) accurate, and these changes of accuracies (caused by the increase of $\partial_z x_c$ from 0 to 0.5) are seen mainly for $z' > 1$ km and become increasingly large as $z'$ increases above 1 km. Similar changes of accuracies have been seen and explained in terms of CRE when the results in Table 4 were compared with those in Table 2.

Figure 6a shows that the diagnosed $V_T^{s+}$ and $(V_R^{s+}, w^{s+})$ in E-u-1 match their respective benchmark fields reasonably well. Figures 6b and 6c show that the analyzed $(u', v')$ (or $w'$) in E-u-1 matches its benchmark field very closely (or reasonably well) at $z' = 1$ and 4 km, respectively. When the innovations are given by $(-u^i, v^i)$ instead of $-u^i$, the diagnosed $V_T^{s+}$ and $(V_R^{s+}, w^{s+})$ and analyzed $(u', v')$ and $w'$ (not shown) are much closer to their respective benchmark fields than those in Figs. 6a–c. Thus, when the vortex becomes slanted eastward, the single-step analysis performs very well with the idealized dual-Doppler innovations and reasonably well with the idealized single-Doppler innovations, whereas the two-step analysis underperforms the single-step analysis (except for single-Doppler scans perpendicular to the vortex slanting direction).

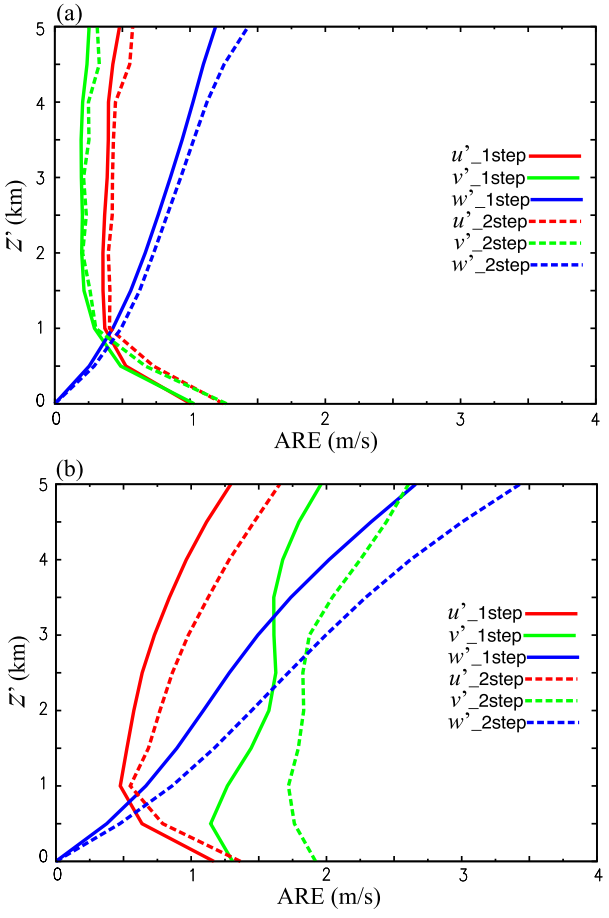


FIG. 5. As in Figs. 3a and 3b, but for eastward-slanted vortex (with $\partial_z x_c = 0.5$ and $\partial_z y_c = 0$).

## 5. Experiments with pseudo-operational Doppler scans from radars A and B

### *a. Results for upright vortex*

For the experiments performed with pseudo-operational Doppler scans of the upright vortex, the resulting CREs are listed in Tables 5 and 6 . As shown by comparing row 1 with row 2 in Table 5, the CREs of analyzed $(V_T^s, V_R^s)$ in E-AB-2 are smaller than $\sigma_o$ but larger than those in E-AB-1, the CRE of analyzed $w^s$ in E-AB-2 is larger than $\sigma_o$ but smaller than that in E-AB-1, and the CREs of diagnosed $(V_T^{s+}, V_R^{s+}, w^{s+})$ in E-AB-2 are all further reduced below $\sigma_o$ but slightly larger than those in E-AB-1. Thus, the axisymmetric part of VF is diagnosed slightly more accurately in E-AB-1 than in E-AB-2. As shown by comparing row 1 with row 2 in Table 6, the CREs of analyzed $(u', v')$ in E-AB-2 are smaller than $\sigma_o$ but slightly larger than those in E-AB-1 whereas the CRE of analyzed $w'$ in E-AB-2 is smaller than that in E-AB-1. Thus, in this case, the two-step analysis is more accurate (or slightly less accurate) than the single-step analysis in analyzing $w'$ [or analyzing $(u', v')$ and diagnosing $(V_T^{s+}, V_R^{s+}, w^{s+})$].

Note that the CREs of analyzed $(u', v', w')$ from E-AB-2 (or E-AB-1) in Table 6 are substantially smaller than those from E-uv-2 (or E-uv-1) in Table 2 and so are the associated RCREs. These CRE reductions can be expected because the pseudo-operational Doppler scans have much higher data density and data coverage than the idealized Doppler scans. Note also that $w'$ is not directly observed from the idealized dual-Doppler scans of the upright vortex but now becomes partially observed from the pseudo-operational Doppler scans because $\theta$ is now not only nonzero but also can be large and so is the projection of $w'$ ($=w$ for upright vortex) on $v_r^o$ [see (2.3)]. This provides an additional explanation for the CRE reduction of analyzed $w'$ in E-AB-2 (or E-AB-1) versus that in E-uv-2 (or E-uv-1).

When the dual-Doppler innovations from radars A and B reduce to single-Doppler innovations from radar A only, the analyzed $(V_T^s, V_R^s, w^s)$ and diagnosed $(V_T^{s+}, V_R^{s+}, w^{s+})$ become less accurate especially for the two-step analysis [as seen from

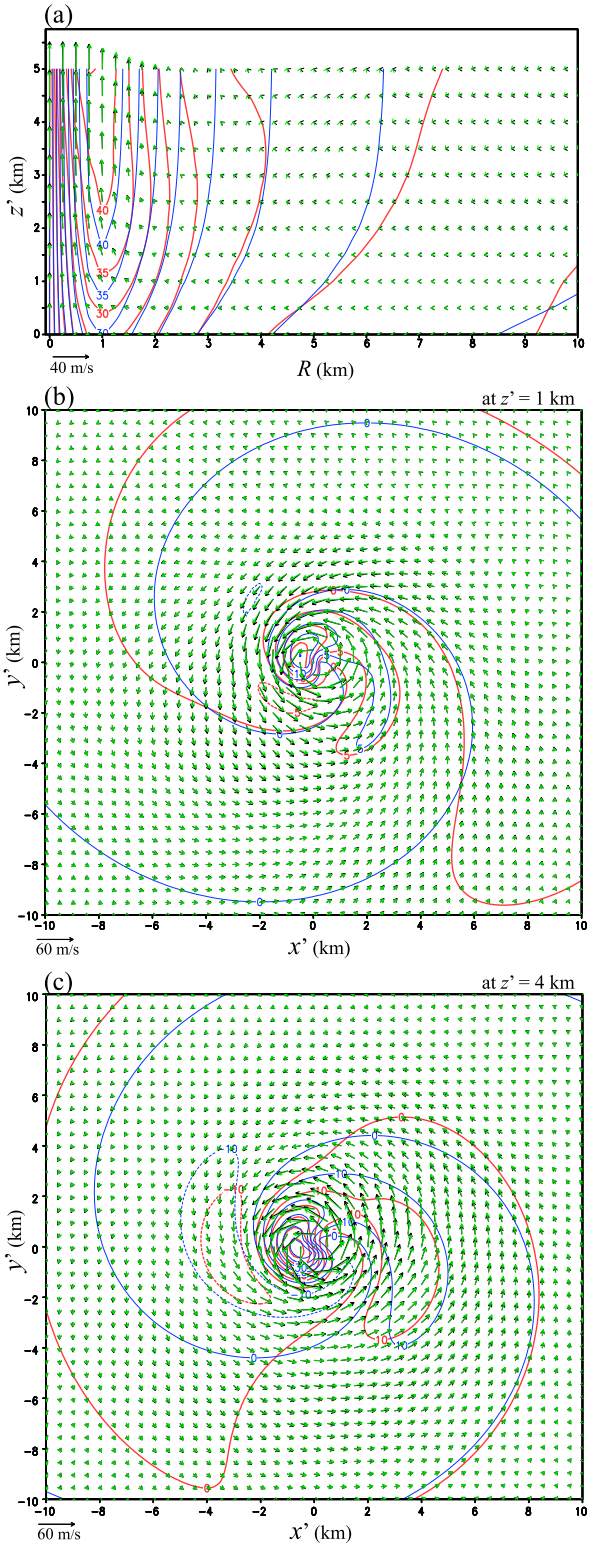


FIG. 6. (a) As in Fig. 1a, but overlapped by diagnosed $V_T^{s+}$ and $(V_R^{s+}, w^{s+})$ from E-u-1 plotted by red contours and green arrows, respectively. (b),(c) As in Figs. 4b and 4c, but from E-u-1. E-u-1 is performed with idealized Doppler scans of eastward-slanted vortex.

TABLE 5. As in Table 1, but from experiments performed with pseudo-operational Doppler scans of upright vortex in section 5a. As described in section 3b, each experiment is named in three parts. The letter "AB," "A," or "B" in the middle part means that the experiment is performed with the dual-Doppler innovations from radar A and radar B, the single-Doppler innovations from radar A only, or the single-Doppler innovations from radar B only. The number "1" (or "2") in the last part means that the experiment is performed by applying the two-step analysis (or single-step analysis).

| Expt | $V_T^s$ | $V_R^s$ | $w^s$ | $V_T^{s+}$ | $V_R^{s+}$ | $w^{s+}$ |
|---|---|---|---|---|---|---|
| E-AB-2 | 0.923 | 0.810 | 1.606 | 0.386 | 0.160 | 0.534 |
| E-AB-1 | 0.286 | 0.442 | 1.873 | 0.250 | 0.130 | 0.493 |
| E-A-2 | 0.975 | 1.331 | 1.797 | 0.932 | 0.442 | 0.884 |
| E-A-1 | 0.820 | 0.601 | 1.671 | 0.672 | 0.226 | 0.463 |
| E-B-2 | 1.377 | 0.978 | 2.195 | 1.376 | 0.559 | 0.711 |
| E-B-1 | 0.982 | 0.577 | 2.012 | 0.871 | 0.218 | 0.381 |

row 3 vs row 1 in Table 5]. The analyzed $(u', w')$ also become less accurate and the analyzed $v'$ becomes much less accurate [as seen from row 3 (or row 4) vs row 1 (or row 2) in Table 6]. The reduced accuracy in analyzed $v'$ can be explained by the largely diminished projections of $v'$ [$=v_v$ for the upright vortex as shown in (2.4)] on $v_r^i$ for single-Doppler innovations from radar A. In this case, the diagnosed $(V_T^s, V_R^s, w^s)$ and analyzed $(u', v', w')$ in E-A-1 are more accurate than those in E-A-2, so the single-step analysis outperforms the two-step analysis.

The same behavior that is seen for radar A is replicated when radar B is considered alone (see row 5 and row 6 in Tables 5 and 6), except in this scenario, the analyzed $u'$ (instead of $v'$) becomes much less accurate [as seen from row 5 (or row 6) vs row 1 (or row 2) in Table 6]. The reduced accuracy in analyzed $u'$ can be explained by the largely diminished projections of $u'$ ($=u_v$ for the upright vortex) on $v_r^i$ for single-Doppler innovations from radar B. In this case, the diagnosed $(V_T^s, V_R^s, w^s)$ and analyzed $(u', v', w')$ in E-B-1 are more accurate than those in E-B-2, so the single-step analysis still outperforms the two-step analysis.

The AREs of analyzed $(u', v', w')$ from the above three pairs of experiments are shown in Figs. 7a–c. As shown in Fig. 7a, the AREs of analyzed $(u', v')$ from E-AB-2 are very close to those from E-AB-1 and the CRE of analyzed $w'$ from E-AB-2 is slightly smaller than that from E-AB-1. These comparisons are consistent with those seen for CREs in row 1 versus row 2 in Table 6. The AREs of analyzed $(u', v', w')$ in Fig. 7a vary with $z'$ similarly to those in Fig. 3a and these vertical variations can be explained similarly (as explained for Fig. 3a in section 4a) except for the following differences: (i) The AREs of analyzed $(u', v')$ in Fig. 7a start to increase not as $z'$ decreases to 1 km (as seen in Fig. 3a) but as $z'$ further decreases below 0.5 km, and this difference can be explained by the fact that observations are now available between $z' = 0.5$ and 1 km from the pseudo-operational Doppler scans. (ii) The AREs of analyzed $(u', v')$ in Fig. 7a do not stay nearly constant (as seen in Fig. 3a) but increase slowly (or substantially) as $z'$ increases above 2.5 (or 4.5) km, and this difference can be explained by the fact that the projection of $(u', v')$ [$=(u_v, v_v)$ for the upright vortex] on $(u^i, v^i)$ is independent of $z'$ but its projection on $v_r^i$ is affected by $z'$.

TABLE 6. As in Table 2, but from experiments performed with pseudo-operational Doppler scans of upright vortex in section 5a.

| Expt | CRE (m s$^{-1}$) | | | RCRE (%) | | |
|---|---|---|---|---|---|---|
| | $u'$ | $v'$ | $w'$ | $u'$ | $v'$ | $w'$ |
| E-AB-2 | 0.420 | 0.486 | 1.663 | 2.8 | 3.2 | 17.7 |
| E-AB-1 | 0.416 | 0.447 | 1.940 | 2.7 | 2.9 | 20.6 |
| E-A-2 | 0.731 | 3.288 | 3.570 | 4.8 | 21.6 | 37.9 |
| E-A-1 | 0.591 | 2.173 | 2.899 | 3.9 | 14.3 | 30.8 |
| E-B-2 | 4.683 | 0.972 | 4.740 | 30.9 | 6.4 | 50.4 |
| E-B-1 | 3.924 | 0.770 | 3.531 | 25.9 | 5.1 | 37.5 |

In particular, as $z'$ increases above 2.5 (or 4.5) km, cos$\theta$ decreases slowly (or substantially) and so does the projection of $(u', v')$ on $v_r^i$ according to (2.3)–(2.4). The increased elevation angle required for analyzing the flow at and above $z' = 2.5$ and 4.5 km implies that $(u', v')$ are being less detected but the detection of $w'$ is increasing. (iii) The AREs of analyzed $(u', v', w')$ in Fig. 7a are substantially smaller than those in Fig. 3a [except for $(u', v')$ above $z' = 4.5$ km], and this is consistent with the earlier explained difference of CREs in the first two rows of Table 6 versus those in Table 2. As shown by the green solid (or dashed) curve in Fig. 7b versus that in Fig. 7a, the ARE of analyzed $v'$ from E-A-1 (or E-A-2) is much larger than that from E-AB-1 (or E-AB-2), and this is consistent with the earlier explained increase of CRE in row 4 (or row 3) from that in row 2 (or row 1) of Table 6. As shown by the red solid (or dashed) curve in Fig. 7c versus that in Fig. 7a, the ARE of analyzed $u'$ from E-B-1 (or E-B-2) is much larger than that from E-AB-1 (or E-AB-2), and this is consistent with the earlier explained increase of CRE in row 6 (or row 5) from that in row 2 (or row 1) of Table 6.

Figure 8a shows that the diagnosed $V_T^{s+}$ and $(V_R^{s+}, w^{s+})$ in E-A-1 match their respective benchmark fields quite closely. Figures 8b and 8c show that the analyzed $(u', v')$ (or $w'$) in E-A-1 matches its benchmark field very closely (or reasonably well) at $z' = 1$ and 4 km, respectively. When the innovations are given from both radar A and radar B (instead of radar A only), the diagnosed $V_T^{s+}$ and $(V_R^{s+}, w^{s+})$ and analyzed $(u', v')$ and $w'$ (not shown) become much closer to their respective benchmark fields than those in Figs. 8a–c. Thus, when the vortex is upright, the single-step analysis performs very well with the dual-Doppler innovations from radars A and B and reasonably well with single-Doppler innovations from either radar A or B. In this case, the two-step analysis underperforms the single-step analysis in general except for analyzing $w^s$ and $w'$ with the dual-Doppler innovations.

### b. *Results for slantwise vortex*

For the experiments performed with pseudo-operational Doppler scans of the eastward-slanted vortex, the resulting CREs are listed in Tables 7 and 8 . As shown in row 1 of Table 7 for the two-step analysis in E-AB-2, the CREs of analyzed $(V_T^s, V_R^s, w^s)$ and diagnosed $(V_T^{s+}, V_R^{s+}, w^{s+})$ become larger when compared to the upright vortex (see row 1 of Table 5). As shown in row 1 of Table 8, the CREs of analyzed $(u', v')$ also become larger but the CRE of analyzed $w'$ becomes smaller

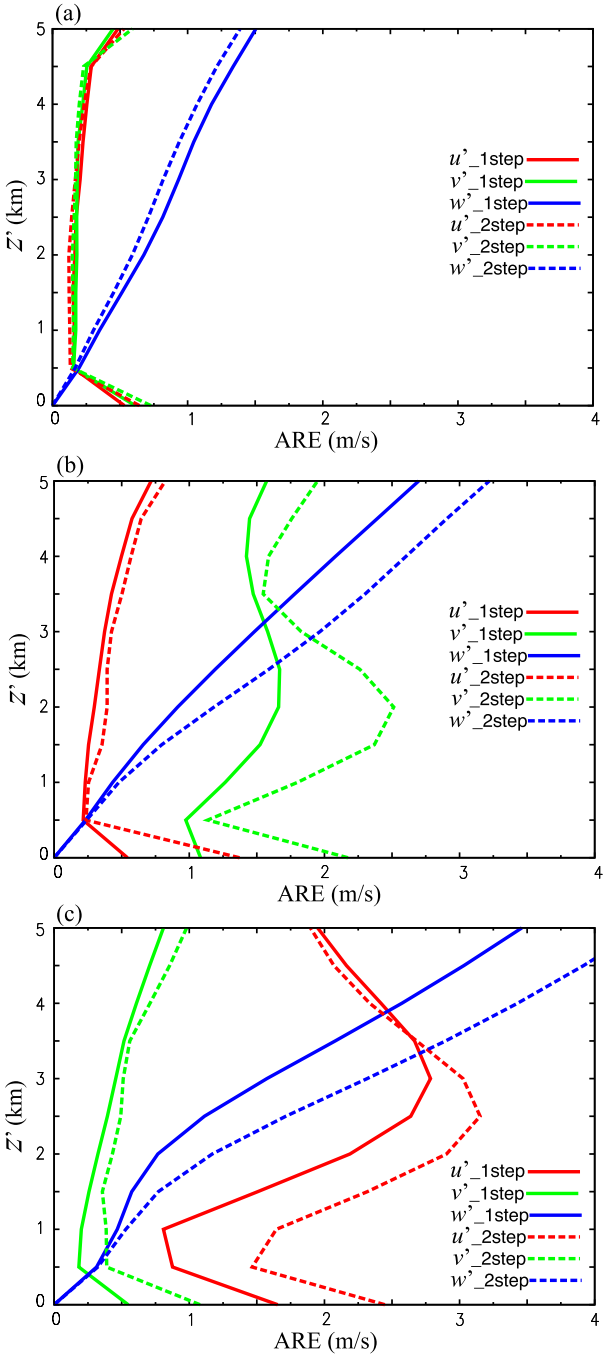


FIG. 7. As in Fig. 3, but from three paired experiments performed with pseudo-operational Doppler scans of upright vortex: (a) E-AB-1 vs E-AB-2 for dual-Doppler analyses, (b) E-A-1 vs E-A-2 for single-Doppler analyses with observations from radar A only, and (c) E-B-1 vs E-B-2 for single-Doppler analyses with observations from radar B only.

when compared to the upright vortex (see row 1 of Table 6). Thus, when the vortex becomes slanted, the axisymmetric part of VF becomes more difficult to analyze and diagnose, and the analyzed $(u', v')$ become less accurate but the analyzed $w'$

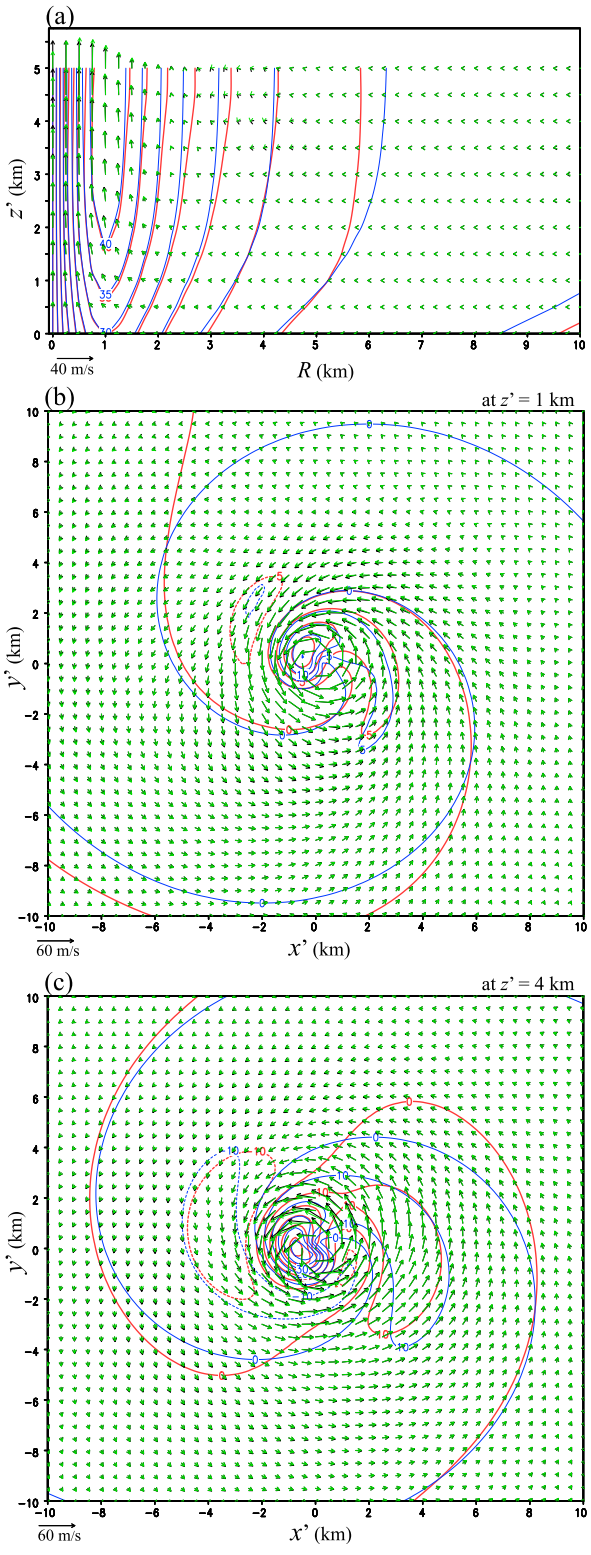


FIG. 8. As in Fig. 6, but from E-A-1 performed with operational Doppler scans of upright vortex.

TABLE 7. As in Table 1, but from experiments performed with operational Doppler scans of eastward-slanted vortex in section 5b.

| Expt | $V_T^s$ | $V_R^s$ | $w^s$ | $V_T^{s+}$ | $V_R^{s+}$ | $w^{s+}$ |
|---|---|---|---|---|---|---|
| E-AB-2 | 1.758 | 1.461 | 2.377 | 0.567 | 0.312 | 0.772 |
| E-AB-1 | 0.361 | 0.526 | 1.467 | 0.337 | 0.175 | 0.586 |
| E-A-2 | 2.508 | 2.513 | 2.980 | 1.762 | 0.629 | 1.191 |
| E-A-1 | 1.158 | 0.781 | 1.560 | 1.100 | 0.391 | 0.560 |
| E-B-2 | 1.574 | 1.246 | 3.676 | 1.604 | 0.496 | 1.329 |
| E-B-1 | 1.036 | 0.573 | 2.081 | 0.946 | 0.216 | 0.392 |

becomes more accurate for the two-step analysis in E-AB-2, and these changes can be explained by the decreased detection of $(u', v')$ and increased detection of $w'$ for the slanted vortex. On the other hand, as shown in row 2 of Table 7 for the single-step analysis in E-AB-1, the analyzed $(V_T^s, V_R^s, w^s)$ and diagnosed $(V_T^{s+}, V_R^{s+}, w^{s+})$ are substantially more accurate than those from the two-step analysis in E-AB-2 (see row 1 of Table 7). As shown in row 2 versus row 1 of Table 8, the analyzed $(u', v')$ in E-AB-1 are more accurate than those from the two-step analysis in E-AB-2 but the analyzed $w'$ in E-AB-1 is slightly less accurate than that from the two-step analysis in E-AB-2. Thus, in this case, the single-step analysis is substantially more accurate than the two-step analysis in analyzing $(V_T^s, V_R^s, w^s)$ and diagnosing $(V_T^{s+}, V_R^{s+}, w^{s+})$ but slightly more (or less) accurate than the two-step analysis in analyzing $(u', v')$ (or $w'$).

When the dual-Doppler innovations from radars A and B reduce to single-Doppler innovations from radar A, the analyzed $(V_T^s, V_R^s, w^s)$ and diagnosed $(V_T^{s+}, V_R^{s+})$ become less accurate (as seen from rows 3 and 4 vs rows 1 and 2, respectively, in Table 7) but the diagnosed $w^{s+}$ become slightly more (or less) accurate for the single-step (or two-step) analysis [as seen from row 3 (or row 4) vs rows 1 (or row 2) in Table 7]. In this case, the analyzed $(u', v', w')$ also become less accurate (as seen from rows 3 and 4 vs rows 1 and 2, respectively, in Table 8). Thus, when the dual-Doppler innovations reduce to single-Doppler innovations from radar A, the axisymmetric part of VF becomes more difficult to analyze and diagnose, the analyzed $(u', w')$ become less accurate, and the analyzed $v'$ becomes much less accurate (due to the reduced projection of $v'$ on $v_r^i$ for single-Doppler innovations from radar A). In this case, the single-step analysis outperforms the two-step analysis.

When the dual-Doppler innovations (from radars A and B) reduce to single-Doppler innovations from radar B, the axisymmetric part of VF also becomes more difficult to diagnose especially for the two-step analysis (as seen from row 5 versus row 1 in Table 7), the analyzed $(v', w')$ become less accurate and the analyzed $u'$ becomes much less accurate (due to the reduced projection of $u$ on $v_r^o$ for each single-Doppler observation from radar B) as seen from rows 5 and 6 versus rows 1 and 2, respectively, in Table 8. In this case, the single-step analysis outperforms the two-step analysis.

Figure 9a shows that the AREs of analyzed $(u', v', w')$ from the paired E-AB-1 and E-AB-2 vary with $z'$ similarly to those in Fig. 7a, and their vertical variations can be explained similarly (to those given for Fig. 7a in section 5a). As $z'$

TABLE 8. As in Table 2, but from experiments performed with pseudo-operational Doppler scans of eastward-slanted vortex in section 5b.

| Expt | CRE (m s$^{-1}$) | | | RCRE (%) | | |
|---|---|---|---|---|---|---|
| | $u'$ | $v'$ | $w'$ | $u'$ | $v'$ | $w'$ |
| E-AB-2 | 0.629 | 0.642 | 1.496 | 4.2 | 4.2 | 15.9 |
| E-AB-1 | 0.542 | 0.443 | 1.521 | 3.6 | 2.9 | 16.2 |
| E-A-2 | 1.354 | 4.225 | 4.149 | 8.9 | 27.7 | 44.1 |
| E-A-1 | 0.913 | 2.360 | 2.641 | 6.0 | 15.5 | 28.1 |
| E-B-2 | 4.720 | 1.083 | 4.831 | 31.2 | 7.1 | 51.3 |
| E-B-1 | 3.865 | 0.843 | 3.407 | 25.5 | 5.5 | 36.2 |

increases above 0.5 km, however, the AREs of analyzed $(u', v')$ in Fig. 9a increase slightly more rapidly but the analyzed $w'$ in Fig. 9a increases less rapidly than those in Fig. 7a, and this difference can be explained by the fact that the projection of $(u', v')$ [$=(u_v$–$w'\partial_z x_c, v_v)$ in this case] on $v_r^o$ decreases but the projection of $w'$ on $v_r^o$ increases as $\partial_z x_c$ increases from 0 to 0.5, as shown in (2.3). Figure 9b shows that the ARE of analyzed $v'$ from E-A-1 (or E-A-2) is much larger than that from E-AB-1 (or E-AB-2), and this is consistent with the earlier explained increase of CRE seen in row 4 (or row 3) versus row 2 (or row 1) in Table 8. Figure 9c shows that the ARE of analyzed $u'$ from E-B-1 (or E-B-2) is much larger than that from E-AB-1 (or E-AB-2), and this is consistent with the earlier explained increase of CRE seen in row 6 (or row 5) versus row 2 (or row 1) in Table 8. The difference between Figs. 9b and 7b is significant because the single-Doppler innovations from radar A are strongly affected by the eastward slanting of the vortex (with $\partial_z x_c$ increased from 0 to 0.5), but the difference between Figs. 9c and 7c is much less significant because the single-Doppler innovations from radar B (to the south of the vertex) are not much affected by the eastward slanting of the vortex.

Figure 10a shows that the diagnosed $V_T^{s+}$ and $(V_R^{s+}, w^{s+})$ in E-A-1 match their respective benchmark fields quite closely. Figures 10b and 10c show that the analyzed $(u', v')$ (or $w'$) in E-A-1 matches its benchmark field very closely (or reasonably well) at $z' = 1$ and 4 km, respectively. When the innovations are from both radar A and radar B (instead of radar A only), the diagnosed $V_T^{s+}$ and $(V_R^{s+}, w^{s+})$ and analyzed $(u', v')$ and $w'$ become much closer to their respective benchmark fields than those in Figs. 10a–c. Thus, when the vortex becomes slanted eastward, the single-step analysis performs very well with the dual-Doppler innovations from radars A and B and reasonably well with single-Doppler innovations from radar A or B, whereas the two-step analysis underperforms the single-step analysis for single-Doppler scans but not for dual-Doppler scans. However, the single-step analysis as well as the two-step analysis performed with single-Doppler innovations from radar B are not much affected by the vortex eastward slanting (as seen and explained above when Fig. 9c is compared with Fig. 7c).

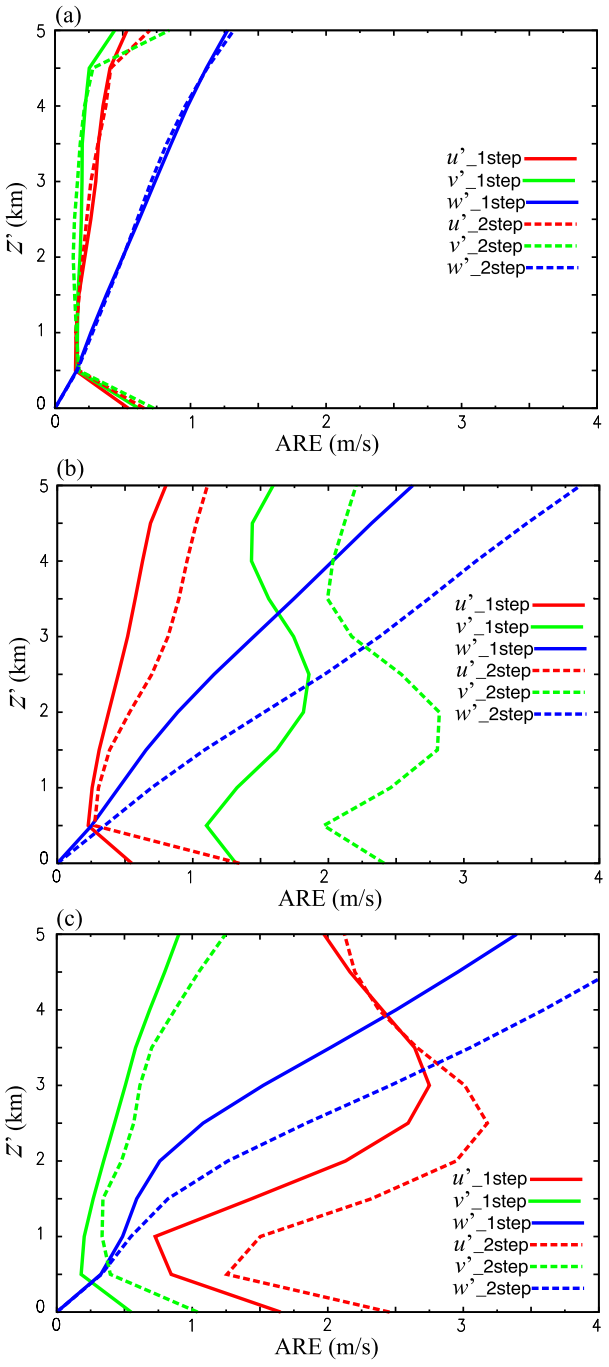


FIG. 9. As in Fig. 7, but for eastward-slanted vortex.

## 6. Conclusions

In this paper, the VF-Var formulated in Part I is tested with simulated dual-Doppler and single-Doppler observations of analytically formulated benchmark vortices. The tangential velocity of the axisymmetric part of benchmark vortex flow (VF) is formulated by extending the parametric model of Vatistas et al. (1991) from the one-dimensional space of $R$ to the two-dimensional space of $(R, z')$, where $R$ is the radial distance from the vortex center and $z'$ is the vertical coordinate along the vortex center axis in the transformed vortex-following coordinate system [see (2.1) of Part I]. The parametric model is also extended to formulate the cylindrical streamfunction of

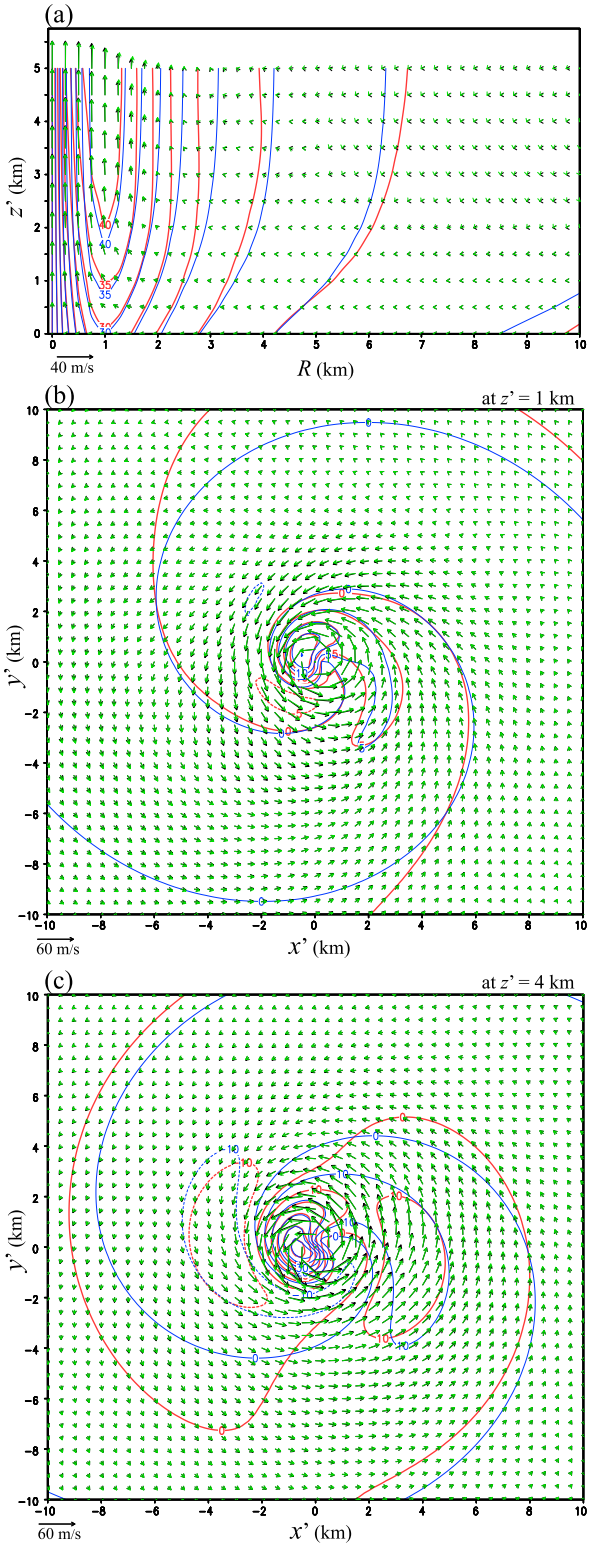


FIG. 10. As in Fig. 8, but for eastward-slanted vortex.

density-weighted vertical circulation for the axisymmetric part of benchmark VF so that the mass continuity equation and boundary conditions (at $z' = 0$ and along $R = 0$) can be satisfied and the angular momentum conservation can be satisfied approximately outside the vortex corner region. The asymmetric part of benchmark VF is formulated analytically also to satisfy the mass continuity equation and boundary conditions.

Simulated radial-velocity observations are generated by applying idealized and pseudo-operational Doppler scans to upright and eastward slantwise benchmark vortices. The idealized Doppler scans are purely horizontal and their generated innovations are simply $-u$ (or $v$) component velocities on a coarse grid (with $\Delta x' = \Delta y' = 0.5$ km and $\Delta z' = 1$ km) in the analysis domain. The pseudo-operational Doppler scans mimic a scan mode used by operational WSR-88Ds for severe storms. Paired experiments are designed and performed to test and compare the two-step analysis versus single-step analysis formulated in VF-Var with simulated radial-velocity observations. The results of these experiments are summarized below:

(i) Both analyses perform very well with dual-Doppler scans and reasonably well with single-Doppler scans, and errors in the analyzed velocities from single-Doppler scans are mainly in the unobserved velocity components and only in fractions of the benchmark velocities.

(ii) For idealized Doppler scans of upright vortex, the two-step analysis outperforms the single-step analysis especially in analyzing the axisymmetric part of VF (see Tables 1 and 2 and Figs. 3 and 4). When the vortex becomes slanted along or against the direction (or one direction) of idealized single-Doppler (or dual-Doppler) scans, the single-step analysis outperforms the two-step analysis (see Tables 3 and 4 and Figs. 5 and 6). In this case, both analyses become less accurate in diagnosing the axisymmetric part and analyzing the horizontal velocity of VF but more accurate in analyzing the slantwise vertical velocity of VF. For idealized single-Doppler scans perpendicular to the vortex slanting direction, the vortex slanting does not affect the analyses. This is because the projection of analyzed slantwise vertical velocity on each radar beam of Doppler scan is zero and thus the velocity observations are not affected by the vortex slanting although they are now located in the slantwise coordinates. The impacts of vortex slanting on the analysis accuracies can be explained by considering the projection of analyzed slantwise vertical velocity on the radar beam of idealized Doppler scans (see section 4b).

(iii) The analyses performed with pseudo-operational Doppler scans are more accurate than those performed with idealized Doppler scans because the pseudo-operational Doppler scans have higher data density and data coverage than the idealized Doppler scans. In this case, the two-step analysis outperforms (or underperforms) the single-step analysis slightly in analyzing the vertical (or horizontal) velocity with dual-Doppler scans of upright vortex but underperforms the single-step analysis in all other tested situations (see Tables 5–8 and Figs. 7–10). When the vortex becomes slanted in the direction largely along or against Doppler scans, both analyses become less (or more) accurate in analyzing the

horizontal velocity (or slantwise vertical velocity) of VF. When the vortex becomes slanted in the direction largely perpendicular to the radar beams of single-Doppler scans, the single-Doppler radial-velocity observations are not much affected by the vortex slanting and so do the analysis accuracies. The impacts of vortex slanting on the analysis accuracies can be explained by considering the projections of analyzed velocity (expressed in terms of the covariant basis vectors in the transformed slantwise coordinates) on radar beams in the original Cartesian coordinates (see section 5b).

(iv) When the vortex is slanted, the projection of axisymmetric (or asymmetric) part of slantwise vertical velocity to the asymmetric (or axisymmetric) part of horizontal velocity is nonzero but not counted when the axisymmetric part is analyzed alone in the first step of the two-step analysis. This causes additional errors in the analyzed axisymmetric part which cannot be rectified (or rectified effectively) at (or around) the vortex center in the second step, because the second-step analyzed asymmetric part diminishes rapidly toward the vortex center in the vortex core (see appendix C of Part I). This explains why the two-step analysis underperforms the single-step analysis in most situations (except for idealized scans of upright vortex), although it only slightly underperforms the single-step analysis except for single-Doppler observations of slanted vortices.

(v) Computationally, the two-step analysis is much more efficient than the single-step analysis for the following reasons. First, the axisymmetric part of VF is computed directly and very efficiently in the first step (due to the smallness of its control variable space as explained at the end of section 3 of Part I). Second, when the asymmetric part of VF is computed alone by using the conjugate-gradient descending algorithm in the second step, the descending algorithm converges within 300 iterations, which is much faster than that (often up to 2000 iterations) for computing the asymmetric part jointly with the axisymmetric part of VF in the single-step analysis. The very slow convergence of the single-step analysis is caused by back-and-forth adjustments as the two parts compete information from the same observations. Thus, the two-step analysis is recommended for upright or nearly upright vortices (although it is often slightly less accurate than the single-step analysis), while the single-step analysis is recommended for slanted vortices (as it becomes much more accurate than the two-step analysis). These recommendations are also supported by additional experiments (not shown in this paper) performed with differently slanted one-cell vortices and differently formulated one-cell and two-cell vortices.

The results summarized above will remain essentially the same if the analysis domain is enlarged horizontally (from $20 \times 20$ to $40 \times 40\,\text{km}^2$) or vertically (from $D = 5$ to 10 km), and this is evidenced by our additional experiments (as shown in appendix B). The results will also remain essentially the same if the U.S. standard atmospheric density used in this paper (as the basic-state air density in configuring the benchmark VFs and performing the analyses) is changed, say, to a constant air density (with neutral stratification). This is also evidenced by our additional experiments (as shown in appendix B). However, if the basic-state air density is not correctly specified in the analyses, errors in the basic-state air density used in analyses will cause additional analysis errors. This and related problems are not examined in this paper but subject to our continued studies (by considering and estimating the air density as a function of not only height but also radial distance from the vortex center).

The benchmark vortices configured in this paper are intended to resemble large intense tornadic mesocyclones (observable by operational WSR-88Ds as explained in section 2a and appendix A) but they are assumed stationary in the vortex-following moving coordinate system over the analysis time window. As the analysis time window is set to 5 min (which is a typical volume scan time used by operational WSR-88Ds for severe storms), the stationary-VF assumption can be valid only for a slowly evolving large mesocyclone outside the vortex core but not for a tornado inside the vortex core. For the anticipated future operational phase-array radars with adaptive weather-surveillance capabilities (Zrnić et al. 2007; Heinselman and Torres 2011; Torres et al. 2012, 2013), the phase-array volume scans (or adaptive subvolume scans) can be updated every 1 min (or every 10 s), so the analysis time window can be sufficiently short to validate stationary-VF assumption without affecting the results presented in this paper (because the VF-Var analyzes only the time averaged VFs and the benchmark vortices are assumed stationary).

Currently, the VF-Var is being used to analyze the 3D VF of the 20 May 2013 Oklahoma Newcastle–Moore tornadic mesocyclone observed by the operational KTLX radar and the NSSL experimental phase-array radar (Zrnić et al. 2007). The analyzed 3D VF is being used to improve the initial condition and subsequent short-term prediction of the track and intensity of mesocyclone for a selected ensemble member in the tornado-resolving ensemble predictions of the Newcastle–Moore tornado (Snook et al. 2019) after the mesocyclone in the selected ensemble member is relocated to the estimated location by the three-step method (Xu et al. 2017). The preliminary results are encouraging. We can envision that continued research in this direction hold promise for future operational applications in terms of addressing the issues raised in the introduction of Part I and overcoming the related difficulties in tornadic-storm data assimilation and forecasts.

Real-life tornadic mesocyclones are often smaller than the benchmark vortices and observed in range distances larger than assumed (30 km) in this paper, so they are sampled at coarser or much coarser spatial resolutions than simulated in this paper. According to our additional experiments (not shown in this paper), when the idealized scans are coarsened horizontally twice (to $\Delta x' = \Delta y' = 1$ km), the analysis errors are increased nearly twice for observed velocity components [such as both $u'$ and $v'$ (or $u'$ only)] but increased only slightly for unobserved components [that is, $w'$ only (or both $v'$ and $w'$)]. Similar analysis error responses to coarsened observations are seen for pseudo-operational Doppler scans when the range distance of vortex center from each radar increases (to 60 or even 120 km). Thus, coarsened observations present a serious challenge for applications of the VF-Var even to future operational phase-array adaptive subvolume scans (due to limited range resolutions) unless the scanned vortices are large and in close ranges.

TABLE B1. As in rows 1–4 of Table 1, but obtained with the horizontal area of analysis domain enlarged from 20 × 20 to 40 × 40 km$^2$.

| Expt | $V_T^s$ | $V_R^s$ | $w^s$ | $V_T^{s+}$ | $V_R^{s+}$ | $w^{s+}$ |
|---|---|---|---|---|---|---|
| E-uv-2 | 0.247 | 0.106 | 0.466 | 0.116 | 0.079 | 0.274 |
| E-uv-1 | 0.272 | 0.503 | 1.590 | 0.120 | 0.074 | 0.285 |
| E-u-2 | 0.384 | 0.137 | 0.442 | 0.184 | 0.113 | 0.273 |
| E-u-1 | 0.408 | 0.506 | 1.668 | 0.187 | 0.098 | 0.265 |

TABLE B2. As in rows 1–4 of Table 2, but obtained with the horizontal area of analysis domain enlarged from 20 × 20 to 40 × 40 km$^2$.

| | CRE (m s$^{-1}$) | | | RCRE (%) | | |
|---|---|---|---|---|---|---|
| Expt | $u'$ | $v'$ | $w'$ | $u'$ | $v'$ | $w'$ |
| E-uv-2 | 0.784 | 0.568 | 1.981 | 5.2 | 3.8 | 29.7 |
| E-uv-1 | 0.838 | 0.605 | 2.207 | 5.6 | 4.0 | 33.1 |
| E-u-2 | 0.796 | 1.704 | 1.910 | 5.3 | 11.3 | 28.7 |
| E-u-1 | 0.800 | 1.743 | 1.967 | 5.3 | 11.6 | 29.5 |

However, the VF-Var is developed not only for operational radars but also for research mobile radars. The applicability to mobile radar rapid Doppler scans [with range resolutions finer than 50 m and sector scan updated times shorter than 10 s, as shown in Table 1 of Kurdzo et al. (2017)] can be envisioned from the experiments performed with pseudo-operational Doppler scans in this paper by downscaling the spatial and temporal dimensions 10 times. In this case, the analysis accuracies will remain the same, but the vortex core radius is 100 m (downscaled from 1 km), the range distance from each radar is 3 km, the radar range resolution is 25 m, the volume scan time is 30 s (and so is the analysis time window), and the decorrelation depth and radial length of VF-dependent covariance functions are also downscaled 10 times (and so is the decorrelation arc length). Clearly, by scaling the spatial and temporal dimensions into nondimensional forms, the experiments presented in this paper can represent similar situations over wide ranges of scales including the above envisioned for mobile Doppler scans, although applications to mobile radar observations require continued research beyond this paper. Thus, the VF-Var is scale adaptive and can be applied to high-resolution mobile-radar observations of tornadoes, especially mesocyclone-generated violent tornadoes, to analyze the detailed flow structures of these tornadoes and study the related dynamic processes via combined uses of all available observations.

The VF-Var is tested in this paper by assuming that the vortex center location is accurately estimated. In real radar data applications, the vortex center location estimated from Doppler scans of a tornadic mesocyclone is not free of error [although the error standard deviation can be smaller than the radius of vortex core as shown in Xu et al. (2017)]. It is thus necessary and important to examine the sensitivities of the accuracies of analyses produced by the VF-Var to vortex center location errors. This problem is under our current investigation (with encouraging results) and the results will be presented in a follow-up paper.

*Acknowledgments.* The authors thank Drs. Jidong Gao and Pamela Heinselman at NSSL for reviewing the manuscript internally, and to the anonymous reviewers for their constructive comments and suggestions. The numerical experiments were performed mostly at the OU supercomputer Schooner. The research work was supported by NSSL Warn-on-Forecast project and ONR Grants N000141712375 and N000142012449 to the University of Oklahoma (OU). Funding was also provided to CIMMS by NOAA/OAR under NOAA–OU Cooperative Agreement NA110AR4320072, U.S. Department of Commerce.

## APPENDIX A

### Formulations and Parameter Settings for Benchmark VF

#### *a. Formulations for the axisymmetric part of VF*

For intense atmospheric vortices (such as tornadoes, mesocyclones, and tropical cyclones), the radial profiles of tangential velocity often can be described approximately by continuous functions that increase from zero at $R = 0$ to a maximum at some radius and then decrease asymptotically to zero as $R$ increases infinitely. In this regard, the three-parameter vortex model of Vatistas et al. (1991) is more realistic than the classic two-parameter Rankine vortex model (Rankine 1882) because the radial profile of tangent velocity in the Rankine vortex model has a cusp at the maximum tangent velocity which is formulated for idealized inviscid VFs but unrealistic for VFs in real fluids. This unrealistic cusp is smoothed out as the third parameter $q$ (that controls the sharpness of the peak of tangent velocity profile at the maximum) reduces from infinity to a finite value in the three-parameter model of Vatistas et al. (1991). According to Vatistas et al. (1991), their three-parameter vortex model with $q = 2$ is physically most representative for many real vortex profiles in the field of aerodynamics engineering. In this case, their three-parameter vortex model reduces to a two-parameter vortex model, and this two-parameter vortex model was used effectively to analyze vortex winds from raw aliased radar radial-velocity observations of hurricanes (Xu et al. 2014) and tornadic mesocyclones (Xu and Nai 2017).

By extending the above two-parameter vortex model from the one-dimensional space of $R$ to the two-dimensional space of $(R, z')$ where $R$ is the radial distance from the vortex center and $z'$ is the vertical coordinate along the vortex center axis in the transformed slantwise coordinate system [see (2.1) of Part I], the tangential velocity (defined in section 2b of Part I) for the axisymmetric part of VF can be formulated as a function of $(R, z')$ by

$$V_T^s = 2^{1/2} V_1 R R_1^{-1} \left(\frac{1 + R^4}{R_1^4}\right)^{-1/2} \left[1 + 0.5 \tanh\left(\frac{z'}{h}\right)\right] \quad \text{for} \quad 0 \le z' \le D, \tag{A1a}$$

where $V_1$ is the maximum $V_T^s$ on $z' = 0$, $R_1$ is the radius of maximum $V_T^s$, $h$ is the height of boundary layer, and $D$ is the height of analysis domain (determined by the radar-observed height of VF). The cylindrical streamfunction [defined in (3.2)

TABLE B3. As in rows 1–4 of Table 1, but obtained for domain height increased from $D = 5$ to 10 km.

| Expt | $V_T^s$ | $V_R^s$ | $w^s$ | $V_T^{s+}$ | $V_R^{s+}$ | $w^{s+}$ |
|---|---|---|---|---|---|---|
| E-uv-2 | 0.156 | 0.244 | 0.436 | 0.225 | 0.076 | 0.274 |
| E-uv-1 | 0.240 | 0.077 | 0.495 | 0.234 | 0.077 | 0.420 |
| E-u-2 | 0.277 | 0.094 | 0.624 | 0.284 | 0.127 | 0.501 |
| E-u-1 | 0.303 | 0.435 | 1.830 | 0.287 | 0.151 | 0.581 |

TABLE B4. As in rows 1–4 of Table 2, but obtained for domain height increased from $D = 5$ to 10 km.

| | CRE (m s$^{-1}$) | | | RCRE (%) | | |
|---|---|---|---|---|---|---|
| Expt | $u'$ | $v'$ | $w'$ | $u'$ | $v'$ | $w'$ |
| E-uv-2 | 0.714 | 0.455 | 1.862 | 4.6 | 2.9 | 24.4 |
| E-uv-1 | 0.687 | 0.452 | 1.837 | 4.4 | 2.9 | 24.1 |
| E-u-2 | 0.676 | 2.117 | 3.003 | 4.3 | 13.6 | 39.3 |
| E-u-1 | 0.677 | 2.131 | 3.027 | 4.3 | 13.6 | 39.6 |

of Part I] of density-weighted vertical circulation for the axisymmetric part of VF is formulated by

$$\psi^s = 2^{1/2} V_2 h R R_2^{-1} \left(\frac{1+R^4}{R_2^4}\right)^{-1/2} \tanh\left(\frac{z'}{h}\right) \quad \text{for} \quad 0 \le z' \le D, \tag{A1b}$$

where $V_2$ is the maximum inward radial velocity (defined by $-V_R^s \equiv \partial_z' \psi_s/\rho_a$) on $z' = 0$, $\rho_a$ is the basic-state air density scaled by its value at $z' = 0$, and $R_2$ is the radius of maximum $-V_R^s$ on $z' = 0$. In this paper, $\rho_a$ is computed from the vertical profile of U.S. standard atmospheric density. According to our additional experiments (not shown in this paper), the accuracy of analyzed VF is not much affected by different specifications of $\rho_a$ even when $\rho_a$ is simply set to 1 over the entire depth of analysis domain.

Substituting (A1b) into (3.2) of Part I gives the radial velocity $V_R^s$ and the slantwise-vertical velocity $w^s$ for the axisymmetric part of VF in the following forms:

$$V_R^s \equiv -\frac{\partial_{z'}\psi^s}{\rho_a} = \frac{-2^{1/2} V_2 R R_2^{-1} \left(\frac{1+R^4}{R_2^4}\right)^{-1/2} \left[\cosh\left(\frac{z'}{h}\right)\right]^{-2}}{\rho_a}, \tag{A2a}$$

$$w^s \equiv R^{-1}\frac{\partial_R(R\psi^s)}{\rho_a} = \frac{2^{3/2} V_2 h R_2^{-1} \left(\frac{1+R^4}{R_2^4}\right)^{-3/2} \tanh\left(\frac{z'}{h}\right)}{\rho_a}. \tag{A2b}$$

Note that $\partial_R V_R^s|_{z'=0} = -2^{1/2} V_2 R_2^{-1}(1 - R^4/R_2^4)\ (1 + R^4/R_2^4)^{-3/2}$, so $\partial_R V_R^s|_{z'=0} = 0$ at $R = R_2$, and this verifies that $V_R^s|_{z'=0} = 0$ reaches the minimum of $-V_2$ at $R = R_2$. Note also that $(V_R^s, w^s)$ formulated in (A2) satisfies not only the mass continuity equation [see (3.1) of Part I] but also the two boundary conditions in $(R, z')$, that is, $w^s = 0$ at $z' = 0$ and $V_R^s = V_T^s = 0$ at $R = 0$ (see section 2c of Part I).

For inviscid and axisymmetric VFs in the slantwise cylindrical coordinate system $(R, z')$, one can verify that the angular momentum conservation can be expressed in the same invariant form of $\partial(R\psi^s, RV_T^s)/\partial(R, z') = 0$ as in the vertical cylindrical coordinate system, where $\partial(\ ,\ )/\partial(\ ,\ )$ is the Jacobian differential operator, $RV_T^s$ is the angular momentum and $R\psi^s$ is the Stokes streamfunction. This angular momentum conservation is satisfied or nearly satisfied by the axisymmetric part of VF formulated in (A1)–(A2) outside the corner region (defined by $R \le R_1$ and $z' \le h$). This is evidenced by the fact that the contours of $RV_T^s$ are parallel or nearly parallel to those of $R\psi^s$ (not shown) and thus $\partial(R\psi^s, RV_T^s)/\partial(R, z')$ is zero or nearly zero outside the corner region.

### b. Formulations for the asymmetric part of VF

The density-weighted vertically integrated velocity potential and streamfunction [defined in (4.4) of Part I] for the asymmetric part of VF in the slantwise cylindrical coordinate system $(R, \beta, z')$ are formulated by

$$X = V_3 R_1 h \tanh(z'/h) E(R, \beta, z')] \quad \text{for} \quad 0 \le z' \le D, \tag{A3a}$$

$$Y = -V_4 R_1 \cosh(z/h)^{-2} E(R, \beta, z') \quad \text{for} \quad 0 \le z' \le D, \tag{A3b}$$

where $V_3$ (or $V_4$) is the velocity scale that controls the amplitude of the divergent (or rotational) part of horizontal velocity for the asymmetric part of VF {and, specifically, the radial component of the divergent horizontal velocity [or the tangential component of the rotational horizontal velocity] for the asymmetric part of VF that is formulated by the first term, $V_3 R_1 [\cosh(z'/h)^{-2} E_R + h \tanh(z'/h) E_{Rz}]/\rho_a$, on the right-hand side of (A4b) [or the last term, $-V_4 R_1 \cosh(z'/h)^{-2} E_R/\rho_a$, in (A4a)] as a periodic function of $\beta$ for fixed $(R, z')$ with an amplitude of $1.4V_3$ (or $1.4V_4$) on the circle of $-\pi < \beta \le \pi$ at $R = R_1$ and $z' = 0$},

$$E(R, \beta, z') \equiv (R/R_1)^{5/2} \exp(-R/2R_1) \sum_n \left\{ G(\phi_n/\Phi_a) - G\left[(\phi_n - \pi)/\Phi_a\right] \right\}$$

$$\approx (R/R_1)^{5/2} \exp(-R/2R_1) \left[ G\left(\min_n |\phi_n|/\Phi_a\right) - G\left(\min_n |\phi_n - \pi|/\Phi_a\right) \right],$$

$G(\ ) = \exp[-(\ )^2/2]$ denotes the Gaussian function of $(\ )$, $\sum_n$ denotes the summation over integer $n$ from 0 to $\pm\infty$, $\phi_n \equiv \beta + 2n\pi + \ln(1 + R/R_1) - z'\pi/2D$, $\Phi_a = \pi/3$, and $\min_n|(\ )|$ denote the minimum of $|(\ )|$ over $n$.

TABLE B5. As in rows 1–4 of Table 1, but obtained by setting $\rho_a(z) = 1$.

| Expt | $V_T^s$ | $V_R^s$ | $w^s$ | $V_T^{s+}$ | $V_R^{s+}$ | $w^{s+}$ |
|---|---|---|---|---|---|---|
| E-uv-2 | 0.194 | 0.106 | 0.494 | 0.188 | 0.072 | 0.328 |
| E-uv-1 | 0.209 | 0.629 | 1.673 | 0.181 | 0.084 | 0.295 |
| E-u-2 | 0.260 | 0.107 | 0.449 | 0.272 | 0.138 | 0.379 |
| E-u-1 | 0.295 | 0.532 | 1.417 | 0.270 | 0.164 | 0.342 |

Substituting (A3) into (4.5) of Part I gives the tangential velocity $V_T^a$, radial velocity $V_R^a$ and slantwise-vertical velocity $w^a$ for the asymmetric part of VF in $(R, \beta, z')$ in the following forms:

$$V_T^a = \left(\partial_\beta \partial_{z'} X/R - \partial_R Y\right)/\rho_a = V_3 R_1 \left[\cosh(z'/h)^{-2} E_\beta + h \tanh(z'/h) E_{\beta z}\right]/(R\rho_a) - V_4 R_1 \cosh(z'/h)^{-2} E_R/\rho_a, \tag{A4a}$$

$$V_R^a = \left(\partial_R \partial_{z'} X - \partial_\beta Y/R\right)/\rho_a = V_3 R_1 \left[\cosh(z'/h)^{-2} E_R + h \tanh(z'/h) E_{Rz}\right]/\rho_a + V_4 R_1 \cosh(z'/h)^{-2} E_\beta/(R\rho_a), \tag{A4b}$$

$$w^a = -\left(\partial_R^2 + R^{-1}\partial_R + R^{-2}\partial_\beta^2\right) X/\rho_a = -V_3 R_1 h \tanh(z'/h)\left(E_R/R + E_{RR} + E_{\beta\beta}/R^2\right)/\rho_a, \tag{A4c}$$

where $E_\beta \equiv \partial_\beta E$, $E_{\beta z} \equiv \partial_\beta \partial_{z'} E$, $E_R \equiv \partial_R E$, $E_{Rz} \equiv \partial_R \partial_{z'} E$, $E_{RR} \equiv \partial_R^2 E$, $E_{\beta\beta} \equiv \partial_\beta^2 E$, and the detailed formulations for these derivatives of $E$ are omitted here. One can verify that $(V_T^a, V_R^a, w^a)$ formulated in (A4) satisfies not only the mass continuity equation but also the two boundary conditions in $(R, \beta, z')$, that is, $w^a = 0$ at $z' = 0$ and $V_T^a = V_R^a = w^a = 0$ at $R = 0$ (see section 2c of Part I). Furthermore, one can verify that $\int_{-\pi}^{\pi} E(R, \beta, z')\, d\beta = 0$ and so do $E_\beta$, $E_{\beta z}$, $E_R$, $E_{Rz}$, $E_{RR}$, and $E_{\beta\beta}$ defined and used in (A4). This leads to $(2\pi)^{-1}\int_{-\pi}^{\pi} E(V_T^a, V_R^a, w^a)\, d\beta = (0, 0, 0)$, so the asymmetric part of VF formulated in $(R, \beta, z')$ by $(V_T^a, V_R^a, w^a)$ in (A4) contains no axisymmetric part and therefore is purely asymmetric.

### c. *Parameter settings for benchmark VF*

The benchmark VF that is used to evaluate the accuracies of analyzed VFs is configured by setting $V_1 = 30\,\mathrm{m\,s^{-1}}$, $R_1 = 1\,\mathrm{km}$, $D = 5\,\mathrm{km}$, $V_2 = 5\,\mathrm{m\,s^{-1}}$, and $R_2 = 1.5\,\mathrm{km}$ in (A1) and (A2) for its axisymmetric part and setting $V_3 = V_4 = 5\,\mathrm{m\,s^{-1}}$ in (A3) and (A4) for its asymmetric part, while the height of boundary layer is set to $h = 1\,\mathrm{km}$. These parameter settings are selected based on the previous 2D-VF analyses (Xu et al. 2015b) and recent preliminary 3D-VF analyses for the 20 May 2013 Newcastle–Moore, Oklahoma, tornadic mesocyclone observed by the operational KTLX radar and the NSSL phase-array radar (Zrnić et al. 2007). The preliminary 3D-VF analyses were performed by using the VF-Var formulated in Part I, and the results will be reported in a follow-up paper as the analyses are completed. With the above parameter settings, the benchmark VF is intended to resemble a large intense one-cell tornadic mesocyclone, so that it can have adequate intensity and complexities for the purpose of testing the VF-Var.

TABLE B6. As in rows 1–4 of Table 2, but obtained by setting $\rho_a(z) = 1$.

| | CRE ($\mathrm{m\,s^{-1}}$) | | | RCRE (%) | | |
|---|---|---|---|---|---|---|
| Expt | $u'$ | $v'$ | $w'$ | $u'$ | $v'$ | $w'$ |
| E-uv-2 | 0.740 | 0.524 | 1.689 | 4.9 | 3.5 | 24.8 |
| E-uv-1 | 0.740 | 0.524 | 1.689 | 4.9 | 3.5 | 24.8 |
| E-u-2 | 0.741 | 1.774 | 1.757 | 4.9 | 11.0 | 26.2 |
| E-u-1 | 0.742 | 1.778 | 1.755 | 4.9 | 11.0 | 26.2 |

## APPENDIX B

### Results of Sensitivity Tests from Additional Experiments

The results presented in this paper are insensitive to selections of analysis domain size (as long as the analysis domain covers the concerned vortex and the domain is adequately covered by radar observations). In particular, when the horizontal area of analysis domain is enlarged from $20 \times 20$ to $40 \times 40\,\mathrm{km^2}$, most analyzed velocity component fields become even more accurate, and this is shown by the results in Tables B1 and B2 in comparison with their respective counterpart results in Tables 1 and 2.

The results presented in this manuscript are also insensitive to variations of analysis domain height (as long as the analysis domain covers the concerned vortex and the domain is adequately covered by radar observations). In particular, when the analysis domain height is increased from $D = 5$ to 10 km (and the idealized observations are also extended, every $\Delta z' = 1\,\mathrm{km}$, to 10 km), most analyzed velocity component fields become more accurate, as shown by the results in Tables B3 and B4 in comparison with their respective counterpart results in Tables 1 and 2.

The accuracies of analyzed VFs are insensitive to different specifications of vertical profile of normalized density $\rho_a$. The analyzed VFs become slightly more accurate when $\rho_a(z)$ is modified to neutral stratification [that is, $\rho_a(z) = 1$ over the entire depth of the analysis domain], and this is shown by the results in Tables B5 and B6 in comparison with their respective counterpart results in Tables 1 and 2.

## REFERENCES

Gao, J., and Coauthors, 2013: A real-time weather-adaptive 3DVAR analysis system for severe weather detections and warnings. *Wea. Forecasting*, **28**, 727–745, https://doi.org/10.1175/WAF-D-12-00093.1.

Heinselman, P., and S. Torres, 2011: High-temporal resolution capabilities of the National Weather Radar Testbed Phased-Array Radar. *J. Appl. Meteor. Climatol.*, **50**, 579–593, https://doi.org/10.1175/2010JAMC2588.1.

Kurdzo, J. M., and Coauthors, 2017: Observations of severe local storms and tornadoes with the Atmospheric Imaging Radar. *Bull. Amer. Meteor. Soc.*, **98**, 915–935, https://doi.org/10.1175/BAMS-D-15-00266.1.

Marquis, J. N., Y. P. Richardson, P. M. Markowski, D. Dowell, and J. Wurman, 2012: Tornado maintenance investigated with high-resolution dual-Doppler and EnKF analysis. *Mon. Wea. Rev.*, **140**, 3–27, https://doi.org/10.1175/MWR-D-11-00025.1.

Rankine, W. J. M., 1882: *A Manual of Applied Physics*. 10th ed. Charles Griff and Co., 663 pp.

Snook, N., M. Xue, and Y. Jung, 2019: Tornado-resolving ensemble and probabilistic predictions of the 20 May 2013 Newcastle–Moore EF5 tornado. *Mon. Wea. Rev.*, **147**, 1215–1235, https://doi.org/10.1175/MWR-D-18-0236.1.

Torres, S., and Coauthors, 2012: ADAPTS implementation: Can we exploit phased-array radar's electronic beam steering capabilities to reduce update times? *28th Conf. on Interactive Information and Processing Systems for Meteorology, Oceanography, and Hydrology*, New Orleans, LA, Amer. Meteor. Soc., 6B.3, https://ams.confex.com/ams/92Annual/webprogram/Paper196416.html.

——, and Coauthors, 2013: A demonstration of adaptive weather-surveillance capabilities on the National Weather Radar Testbed Phased-Array Radar. *Int. Symp. on Phased Array Systems and Technology*, Waltham, MA, IEEE, 12.1, https://doi.org/10.1109/ARRAY.2013.6731871.

Vatistas, G. H., V. Kozel, and W. C. Mih, 1991: A simpler model for concentrated vortices. *Exp. Fluids*, **11**, 73–76, https://doi.org/10.1007/BF00198434.

Xu, Q., 2021: A variational method for analyzing vortex flows in radar-scanned tornadic mesocyclones. Part I: Formulations and theoretical considerations. *J. Atmos. Sci.*, **78**, 825–841, https://doi.org/10.1175/JAS-D-20-0158.1.

——, and K. Nai, 2017: Mesocyclone-targeted Doppler velocity dealiasing. *J. Atmos. Oceanic Technol.*, **34**, 841–853, https://doi.org/10.1175/JTECH-D-16-0170.1.

——, L. Wei, W. Gu, J. Gong, and Q. Zhao, 2010: A 3.5-dimensional variational method for Doppler radar data assimilation and its application to phased-array radar observations. *Adv. Meteor.*, **2010**, 797265, https://doi.org/10.1155/2010/797265.

——, Y. Jiang, and L. Liu, 2014: Fitting parametric vortex to aliased Doppler velocities scanned from hurricanes. *Mon. Wea. Rev.*, **142**, 94–106, https://doi.org/10.1175/MWR-D-12-00362.1.

——, L. Wei, K. Nai, S. Liu, R. M. Rabin, and Q. Zhao, 2015a: A radar wind analysis system for nowcast applications. *Adv. Meteor.*, **2015**, 264515, https://doi.org/10.1155/2015/264515.

——, ——, and ——, 2015b: Analyzing vortex winds in radar observed tornadic mesocyclones for nowcast applications. *Wea. Forecasting*, **30**, 1140–1157, https://doi.org/10.1175/WAF-D-15-0046.1.

——, ——, and ——, 2017: A three-step method for estimating vortex center locations in four-dimensional space from radar observed tornadic mesocyclones. *J. Atmos. Oceanic Technol.*, **34**, 2275–2281, https://doi.org/10.1175/JTECH-D-17-0123.1.

Zrnić, D. S., and Coauthors, 2007: Agile-beam phased array radar for weather observations. *Bull. Amer. Meteor. Soc.*, **88**, 1753–1766, https://doi.org/10.1175/BAMS-88-11-1753.